Atmos. Chem. Phys., 25, 7597–7617, 2025
https://doi.org/10.5194/acp-25-7597-2025

Atmospheric Chemistry and Physics
Open Access
EGU

Physical–chemical properties of particles in hailstones from central Argentina

Anthony C. Bernal Ayala[1], **Angela K. Rowe**[1], **Lucia E. Arena**[2,3], **and William O. Nachlas**[4]

[1]Department of Atmospheric and Oceanic Sciences, University of Wisconsin-Madison, Madison, WI, USA
[2]Facultad de Matemáticas, Astronomía, Física y Computación,
Universidad Nacional de Córdoba, Córdoba, Argentina
[3]Observatorio Hidrometereológico de Córdoba, Córdoba, Argentina
[4]Department of Geoscience, University of Wisconsin-Madison, Madison, WI, USA

Correspondence: Anthony C. Bernal Ayala (crespo3@wisc.edu)

Received: 18 October 2024 – Discussion started: 11 November 2024
Revised: 2 April 2025 – Accepted: 29 April 2025 – Published: 18 July 2025

Abstract. This study presents a novel analysis of two hailstones collected in central Argentina to provide insights into the size distribution, composition, and potential sources of non-soluble particles within hailstones. Using this new method, non-soluble particles are trapped beneath a thin layer of polyvinyl resin and analyzed with confocal laser and scanning electron microscopy combined with energy-dispersive spectroscopy, preserving their in situ location and physical characteristics. The study characterized these particles' distribution, shape, and size and identified their elemental composition, which is used to interpret possible source regions. Particles ranged in diameter from our detection limit from 1 to 256 µm, with the largest particles consistently found in the hailstone embryos. Agglomerated mineral and organic particles dominated the elemental composition in both the embryo and outer layers, with the largest agglomerated particle (256 µm) being an organic-rich particle in the embryo of the larger hailstone. The composition and size distribution varied between the two hailstones: one contained agglomerated salt particles (up to 150 µm) in its embryo, traced to a nearby salt lake, while the other contained copper chloride and zinc chloride particles (up to 78 µm) primarily in its outer layers, potentially associated with agrochemicals commonly used for pest control and fertilizer in Argentina. Various local and regional land-use types, including shrublands, mixed vegetation, croplands, and urban areas, were linked to specific types of particles. Therefore, this study highlights the regional influence of various land-use types on hail formation and growth, pointing to the potential impacts of natural and anthropogenic factors on hailstone composition and revealing how particle characteristics vary between the embryo and outer layers of hailstones.

1 Introduction

Falling hailstones are some of the most destructive natural phenomena in convectively active regions of the world, with significant global impacts on agriculture, infrastructure, and local economies. In the United States alone, hailstorm damage has exceeded USD 1 billion annually since 1949 (Changnon, 2008; Sander et al., 2013; Allen et al., 2017; Kumjian et al., 2019), with three billion-dollar hailstorm events recorded in 2018 (Mahoney, 2020). Climate change is expected to exacerbate these impacts by increasing hailstone size despite a potential reduction in hailstorm frequency, leading to greater severity and economic consequences (Raupach et al., 2021). Furthermore, spatial variability in trends, such as increases in hail severity in Europe and Australia versus decreases in North America and East Asia, highlights the need for region-specific studies to better understand these dynamics (Raupach et al., 2021).

Studies have explored how environmental factors affect hail production in deep convective storms through high-resolution modeling (e.g., Kumjian and Lombardo, 2020) and using global inferences of hail occurrence through satellite-based proxies (Cecil and Blankenship, 2012; Ni et al., 2017; Bang and Cecil, 2019; Bruick et al., 2019); however, they often are not verified against hail observations. Even when operational radar data are available with accompanying hail reports, accurately estimating hail sizes from these observations remains challenging (e.g., Murillo and Homeyer, 2019). Much remains unknown about the processes leading to hail growth and environmental controls on hail occurrence and size, particularly outside of the United States (Allen et al., 2020). Furthermore, as climate variability and a warming Earth system influence hail occurrence and intensity, understanding these microphysical processes becomes vital for accurate climate modeling and assessing future hydrological cycles (Allen et al., 2020).

Ice-nucleating particles (INPs) are a subset of environmental aerosols that facilitate ice formation through heterogeneous freezing, owing to the assistance of a non-soluble particle such as mineral dust derived from surface sediments, biological material (e.g., pollen, bacteria, fungal spores, and plankton), and volcanic ash (e.g., Lamb and Verlinde, 2011; Vali et al., 2015). While a range of aerosol types can serve as INPs (Lamb and Verlinde, 2011; Zhao et al., 2019; Burrows et al., 2022), various factors affect particles' ice-nucleating capabilities, including their size, surface topography, and composition including coating (e.g., Kiselev et al., 2017; Holden et al., 2021; Gao et al., 2022). The relationship between particle size and its ability to serve as an INP is complex and depends on multiple factors, including temperature, composition, and surface properties. Larger particles ($> 10\,\mu\mathrm{m}$) generally exhibit higher ice-nucleating efficiency per unit mass because they provide greater surface area and can host diverse mineral or organic phases that promote ice formation (Kanji et al., 2017; Knopf et al., 2018). However, smaller particles ($< 1\,\mu\mathrm{m}$) can dominate ice nucleation at colder temperatures or in environments rich in biological materials. Submicron INPs, such as bacterial fragments or fungal spores, are highly effective ice nucleators, even at relatively warm sub-zero temperatures (-10 to $-15\,^{\circ}\mathrm{C}$), while fine mineral fragments like K-feldspar or quartz nanoparticles are efficient at colder temperatures (-20 to $-30\,^{\circ}\mathrm{C}$) (DeMott et al., 2016; Chen et al., 2021; Beal et al., 2021). Even less is known about the types and concentrations of aerosols involved in hail formation, as the complexity of deep convective storm microphysics, limited observations, and the shortcomings of current models contribute to the inconclusive understanding of the effects of INPs on hail formation and growth.

Studies of collected hailstones around the world have provided some insight into potential INPs involved in hail formation. Michaud et al. (2014) found biological ice nuclei in hailstone embryos in the US Rocky Mountains, while hailstones collected in Slovenia (Šantl-Temkiv et al., 2013) and the triple-border region of Paraná, Brazil, and Argentina (Beal et al., 2021) contained signatures of the respective regions' soil. Other studies point to anthropogenic markers through the presence of microplastics (Kozjek et al., 2023), highlighting the implications of human activity on hail formation. In studying INPs, the historical focus on particles $\leq 10\,\mu\mathrm{m}$ primarily reflects technical limitations rather than theoretical constraints. Early detection methods, such as continuous flow diffusion chambers, employed size-selective impactors to avoid optical misclassification of ice crystals and aerosols, systematically excluding supermicron particles from analysis (Cziczo et al., 2009; DeMott and Prenni, 2010). Practical modeling considerations compounded this instrumental bias, as sub-$10\,\mu\mathrm{m}$ particles dominated atmospheric datasets due to their higher abundance and slower sedimentation rates, leading to parameterizations skewed toward smaller sizes (DeMott et al., 2016). Recent advancements in microfluidic arrays enable the investigation of supermicron INPs, revealing their previously underestimated role in processes like hail embryo formation (Tarn et al., 2018). The analysis techniques in studies like Šantl-Temkiv et al. (2013), Michaud et al. (2014), and Beal et al. (2021) all required melting the hailstones, removing information on non-soluble particle size distribution or composition with respect to the hailstone embryo, and neglecting soluble particles. This present work, using a novel hailstone particle analysis method (Bernal Ayala et al., 2024b), adds to the limited literature on hailstones' composition through analysis of individual non-soluble particles contained within hailstones collected in central Argentina, a global hotspot for hail.

Córdoba Province in Argentina has some of the most intense storms in the world (Zipser et al., 2006) and experiences frequent hail (e.g., Cecil and Blankenship, 2012; Rasmussen et al., 2014) that has destructive impacts on property and agriculture. As such, this region has been the focal point of recent field campaigns collecting data on these severe storms, including the 2018–2019 Cloud, Aerosol, and Complex Terrain Interactions (CACTI; Varble et al., 2021) and 2018 Remote Sensing of Electrification, Lightning, and Mesoscale/Microscale Processes with Adaptive Ground Observations (RELAMPAGO; Nesbitt et al., 2021) near the Sierras de Córdoba (SDC; Fig. 1), a mesoscale mountain range that runs parallel to the Andes in northwest Argentina. A 7-month (austral spring to mid-autumn) survey of CACTI INP measurements (Testa et al., 2021) found that diverse plant communities in nearby areas likely release high amounts of biological and organic particles. Additionally, intensively farmed plains are identified as a significant source of soil dust from post-harvest to late spring, with a combination of bio-particles released by plants and soil dust when crops start growing thus contributing to INP concentrations during this time of year. This CACTI study did not focus on hailstorms, although it is therefore reasonable to hypothesize that hailstones collected in this region would contain particles containing imprints of both biological and agricultural activity.

To explore the influence of particle identity and availability on hailstone formation, microscopy techniques can be ap-

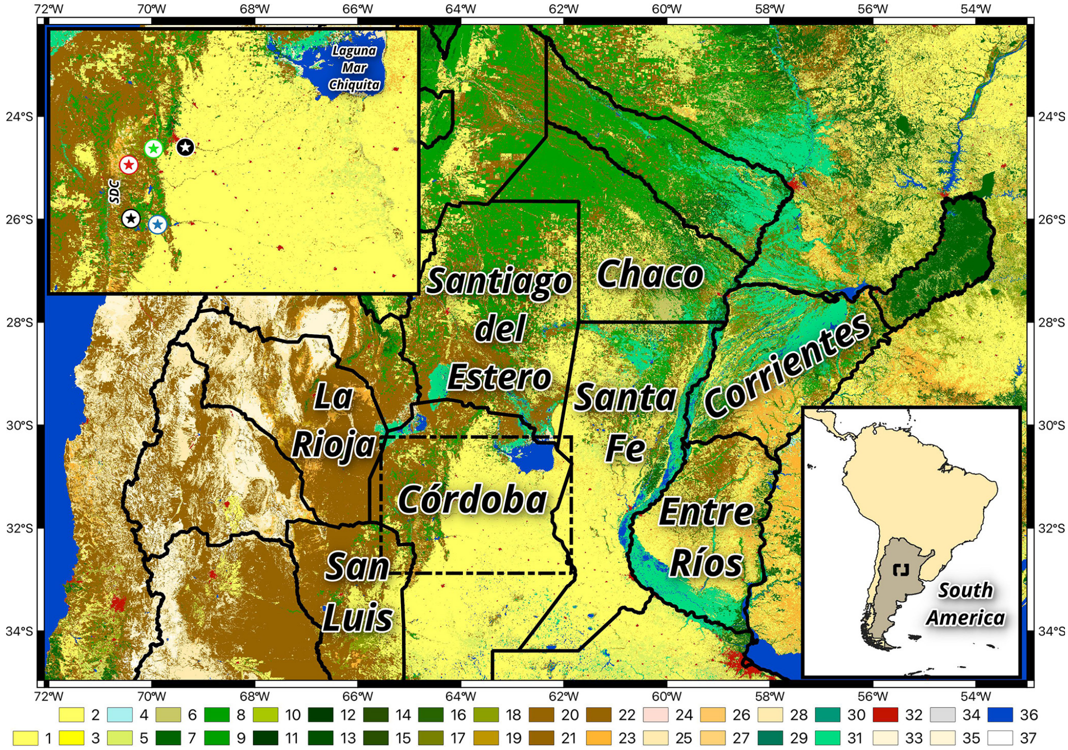

Figure 1. Map of northern Argentina covering an area shown in the black box in the lower right panel, including the Córdoba study area and nearby provinces. Within the dashed box covering northern Córdoba Province is an inset (top left) highlighting the city of Córdoba (white star) to the east of the Sierras de Córdoba (SDC) and points of interest for this analysis: the site of the CACTI experiment observations in Villa Yacanto (black star); the hail collection locations, Villa Carlos Paz and Villa del Dique (lime green and blue stars, respectively); and the initiation point for air mass back-trajectory run for 8 February and 13–14 December (red and blue star, respectively). Color fill represents the C3S Land Cover map available through the C3S Climate Data Store (CDS): 1 – cropland rainfed, 2 – cropland rainfed, 3 – cropland rainfed tree or shrub cover, 4 – cropland irrigated, 5 – mosaic cropland, 6 – mosaic natural vegetation, 6 – tree broadleaved ever- green closed to open, 7 – tree broadleaved deciduous closed to open, 8 – tree broadleaved deciduous closed, 9 – tree broadleaved deciduous open, 10 – tree needle-leaved evergreen closed to open, 11 – tree needle-leaved evergreen closed, 12 – tree needle-leaved evergreen open, 13 – tree needle-leaved deciduous closed to open, 14 – tree needle-leaved deciduous closed, 15 – tree needle-leaved deciduous open, 16 – tree mixed, 17 – mosaic tree and shrub, 18 – mosaic herbaceous, 19 – shrubland, 20 – shrubland evergreen, 21 – shrubland deciduous, 22 – grassland, 23 – lichens and mosses, 24 – sparse vegetation, 25 – sparse tree, 26 – sparse shrub, 27 – sparse herbaceous, 28 – tree cover flooded fresh or brackish water, 29 – tree cover flooded saline water, 30 – shrub or herbaceous cover flooded, 31 – urban, 32 – bare areas, 33 – bare areas consolidated, 34 – bare areas un- consolidated, 35 – water, 36 – snow and ice.

plied to the individual non-soluble particles using the new method described in Bernal Ayala et al. (2024b). Studies over the past two decades (e.g., Sokolik and Toon, 1996; Tegen and Lacis, 1996; Claquin et al., 1999; Sokolik and Toon, 1999; Kandler et al., 2007; Nousiainen et al., 2009; Jeong and Achterberg, 2014; Kemppinen et al., 2015; Li and Sokolik, 2018; Conny et al., 2019; Huang et al., 2020; Di Biagio et al., 2020) have used scanning electron microscopy (SEM) with energy-dispersive X-ray spectroscopy (EDS) to identify and quantify the mineral phases present in dust aerosols. Much of this work has focused on dust samples from desert regions like Asia and the Sahara, identifying key mineral phases including quartz, calcite, halite, and hematite (Jeong and Nousiainen, 2014; Schütz and Sebert, 1987). The mineralogical complexity of dust particles is further compounded by amorphous silica, particularly in Saharan dust, often associated with clay minerals (Jeong et al., 2016). These findings provide a valuable reference framework for interpreting EDS spectra and identifying potential mineral phases in dust samples. However, to fully understand the role of these particles in ice nucleation, it is necessary to investigate their mineralogical composition; physical characteristics; and other factors, including agglomeration of multiple particle types. Previous studies suggest that organic-rich soil dust more efficiently serves as INPs than mineral desert dust (Conen et al., 2011; Steinke et al., 2016; Cornwell et al., 2024), but how much of this enhancement is owing to the presence of organic coatings and biological material remains unclear. With agricultural soil dust and biological particles likely being primary aerosol sources available for hail formation in central Argentina (e.g., Testa et al., 2021), it is crucial to explore the mineral composition of individual particles to understand potential INP sources for hailstone formation.

This study uniquely studies the physical and chemical properties of non-soluble particles retaining their position within each hailstone layer for two hailstorms of varying modes in central Argentina. The overall motivation of this work is to provide insight into which non-soluble particles were likely involved in the initial stages of ice nucleation and thus hail formation and subsequent growth, as well as their potential source regions. The specific objectives of this study are to (1) characterize the distribution and size of non-soluble particles trapped in both hailstone samples, (2) identify the elemental composition distribution of individual non-soluble particles collected by each hailstone during its growth in the cloud, and (3) determine possible source regions of non-soluble particles identified in the hailstones. Section 2 describes the datasets and methods used to address these objectives. Section 3 describes the physicochemical characterization of non-soluble particles found in the hailstone sample. Section 4 discusses the results in the context of previous work and the implications of those results.

2 Data and methods

2.1 Hailstone collection and preparation

The hailstones used for this analysis were collected during two hail events: 8 February and 13–14 December 2018, the latter occurring during the RELAMPAGO-CACTI observation period. More specifically, the 4 cm hailstone from 8 February (hereafter referred to as V-7) was collected in Villa Carlos Paz, Córdoba, Argentina (lime-green star in Fig. 1), and the 8 cm hailstone from 14 December (NG-1) was collected in Villa del Dique, Córdoba, Argentina (blue star in Fig. 1). These collections were facilitated through Lucia E. Arena at the Facultad de Matemática, Astronomía, Física y Computación at the Universidad Nacional de Córdoba (FAMAF-UNC) and the citizen science Cosecheros Program (Arena and Crespo, 2019; Arena, 2022).

Following collection, each hailstone was immediately placed in a nylon bag within a thermally reinforced cooler maintained at −15 °C and assigned a unique alphanumeric identifier incorporating the collector's name. Upon arrival at FAMAF-UNC's subzero facility (Laura Levi Atmospheric Physics Laboratory), the hailstone surface was carefully brushed to remove potential contamination before being transferred to a cold chamber at −12±2 °C for processing. At this stage, a novel approach to preserve non-soluble particles within hail layers was implemented (Arena, 2024; Bernal Ayala et al., 2024b). Hailstone samples were attached to a glass base and then cut over the equatorial symmetric plane using a diamond-embedded cutting disk. After cutting the hailstone to expose the embryo, the sample was evenly polished with a microtome to provide a thin, even ice layer over the embryo. At this stage, pictures were taken to record the location of growth rings relative to the embryo. Immediately after, 1 % polyvinyl formal (Formvar) solution diluted in ethylene dichloride was applied with a glass rod over the flat polished surface and left to curate for a few minutes. Once covered with the Formvar solution, the hailstone was left in a sealed low-humidity container with silica gel at −12 °C to sublimate. Once the ice sublimated, the particles trapped in the Formvar could be analyzed using light and electron microscopy at room temperature while preserving their location with respect to the hail embryo. Unlike traditional melting methods, which would dissolve soluble particles, our sublimation approach potentially preserves both soluble and non-soluble particles, though this study focuses on characterizing non-soluble particles. Through this method, we can observe both the non-soluble particles and deposits of compounds that did not sublimate. More details on these hailstone collection and preparation procedures are provided in Bernal Ayala et al. (2024b).

2.1.1 Microscopy analysis

With particles and their locations with respect to the embryo preserved in Formvar, this method then allows for the application of microscopy techniques to provide information on the physical and chemical characteristics of non-soluble particles within hailstones. Using an OLYMPUS LEXT OLS4000 confocal laser scanning microscope (CLSM), a 2-D cross-section of each of the V-7 and NG-1 hail samples (Figs. 2 and 3, respectively) was created by identifying the embryo and using it as a reference point for scanning regions within and around it. For these two cases, the embryo is identified as the original nucleus through its uniform crystallographic structure under polarized light, contrasting with the radially aligned outer layers (Grenier and Sadok Zair, 1983; Takahashi, 1987). The core's small, equiaxed ice grains share nearly identical *c*-axis orientations, indicating it formed from a single frozen droplet or graupel particle (Takahashi, 1987). This uniformity distinguishes it from the outer shells, where elongated grains align radially outward due to wet accretion (water freezing onto the surface; Takahashi, 1987). The radial alignment of *c* axes in these layers points to concentric growth around the embryo, while the embryo's central position and structural simplicity confirm it as the starting point (Soderholm and Kumjian, 2023). The transition from a single-oriented core to layered shells reflects the hailstone's formation sequence, where the embryo acts as the nucleation site for subsequent accretion (Takahashi, 1987; Soderholm and Kumjian, 2023). Additionally, in porous hailstones, the distribution and size of air bubbles differ significantly between the central zone and the external lobes, providing another distinguishing characteristic between the embryo and outer layers (Lubart and Levi, 1984; Levi et al., 1989, 1991). In the case of the 4 cm V-7 sample, the 2-D cross-section (Fig. 2) covers the embryo (Sectors 4–5) and outer layers in both directions from the embryo to the outermost layers of

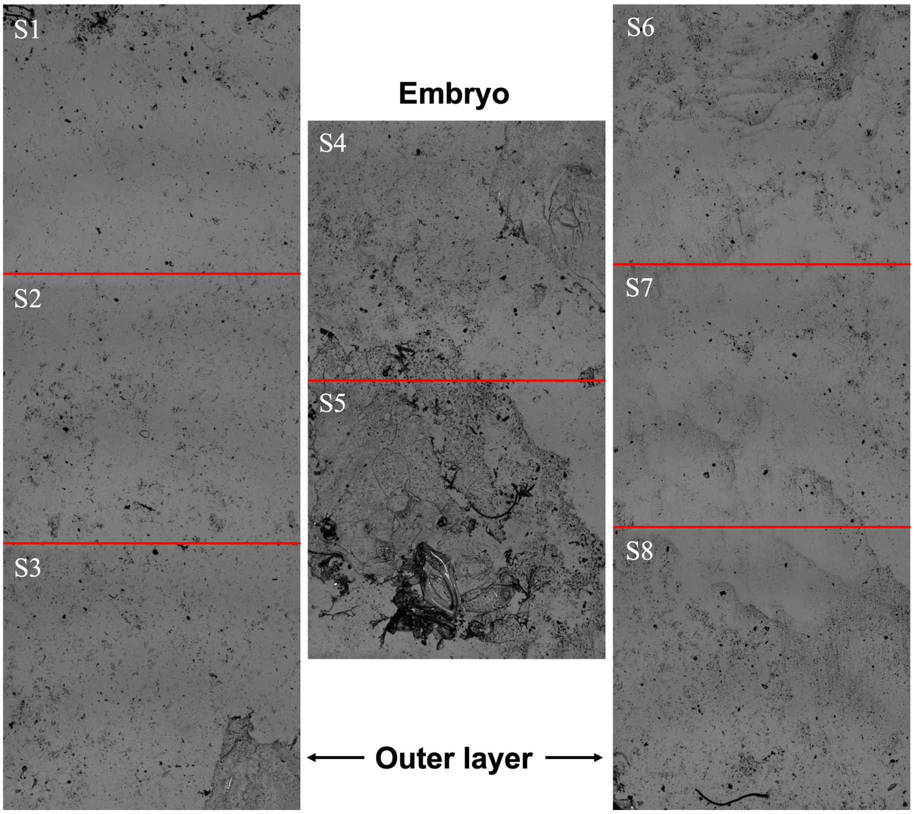

Figure 2. 2-D cross-section along an axis in the equatorial plane at 108 × magnification for sample V-7 collected on 8 February 2018. Sectors (S) 4 and 5 indicate the embryo, while S1–S3 and S6–S8 represent the outer layers.

the stone (Sectors 1–3, Sectors 6–8). Within this 2-D cross-section, individual sectors of equal size (i.e., labeled Sectors 1–8 in V-7, Fig. 2) were selected for higher magnification to identify individual particles quasi-randomly within each sector with respect to the embryo. A similar approach was implemented for NG-1 (Fig. 3); however, owing to the larger size of this stone (8 cm compared to the 4 cm size of V-7), a second CLSM sweep was required to examine the entire area encompassing the embryo. This additional sweep resulted in horizontally adjacent sectors (e.g., Sector 1, Sector 2) in the same vertical section that were then grouped under a similar layer number for analysis (e.g., in Fig. 3, Sector 1 and Sector 2 represented the same layer of the stone and thus were identified as “1” when analyzing particles in that area). These numbered layers cover the larger embryo (1–5) and a cross-section toward one end of the stone identified as the outer layers (6–10).

This approach provided particle size distribution and surface topographical information for 73 and 223 identified particles within the V-7 and NG-1 hailstones, respectively, including particles down to the technique-limited minimum size of 1 µm (Bernal Ayala et al., 2024b). This lower limit is achievable due to the CLSM optical sectioning capability, pinhole aperture design, and high-resolution imaging, which allow for clear visualization of structures approaching the diffraction limit of light without breaking it. It is worth noting that this resolution differs from the SEM, which can achieve resolutions down to 50 nm due to its use of electrons rather than light, offering even finer detail for nanoscale structures. Filmetrics (2017) software was used to calculate particle size, which is determined as the maximum length along the x and y axes. The increase in particle numbers analyzed between the samples is attributed to the increased efficiency in the analysis, allowing for more particles to be examined in a similar amount of time.

The sublimated hailstone samples were then coated with gold (V-7) and gold and palladium (NG-1), the difference owing to the availability of pure gold during lab analysis times and subsequently analyzed using a Zeiss Sigma field emission gun (FEG) SEM with an EDS X-Max 80 mm^2 detector. Secondary electron images were acquired at 15 kV and a working distance of approximately 8.5 mm, settings that dictated the clarity and detail of the imagery and allowed for the identification of heavy metals without disintegrating the non-soluble particles (Bernal Ayala et al., 2024b). The 2-D elemental cross-sectional maps (Figs. 2 and 3) were used to locate the same particles observed in the CLSM to investigate the elemental composition of the same identified individual particles. To minimize interference from the sample substrate, EDS spectra were acquired for 120 s from the

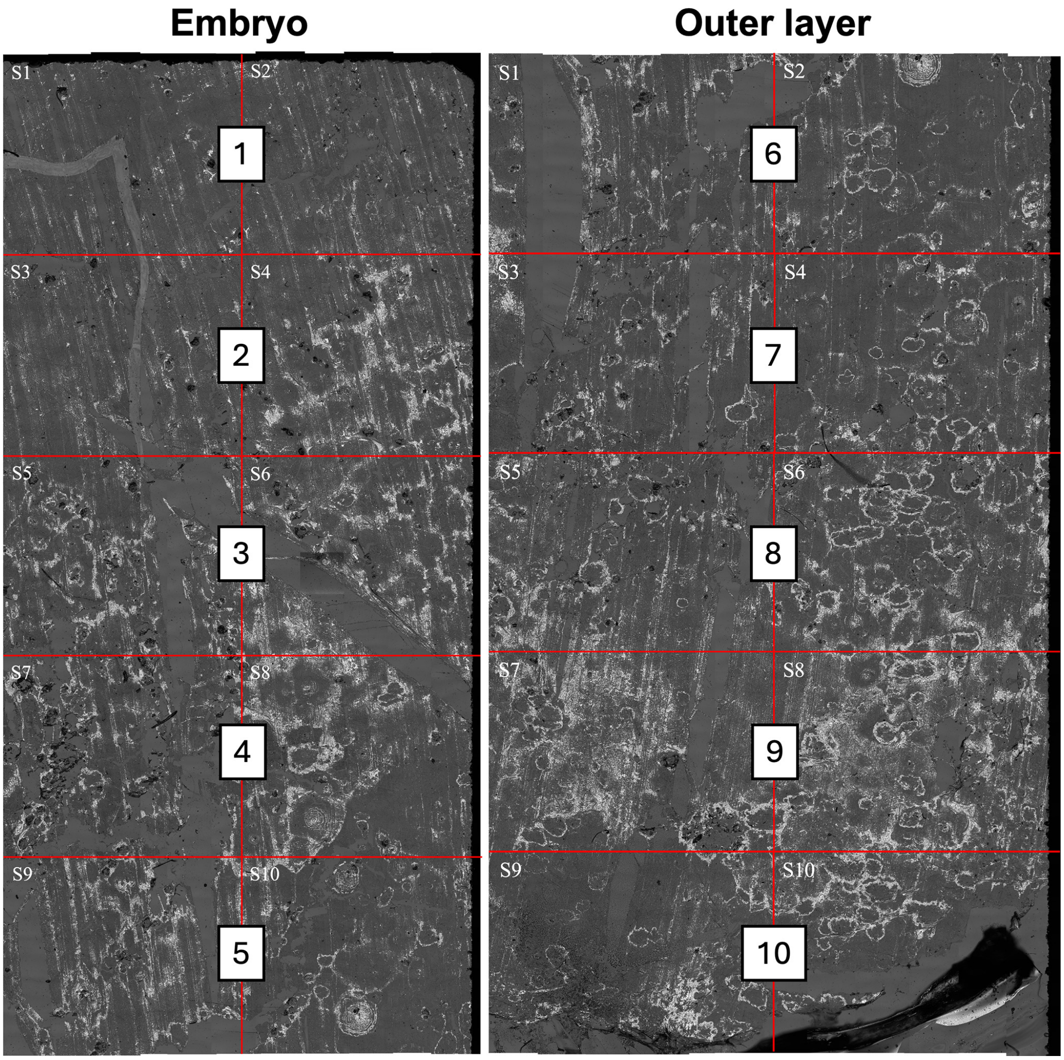

Figure 3. As in Fig. 2, but for NG-1 collected on 13–14 December 2018. Sectors are grouped by layers relative to the embryo (layers 1–5) and outer layer (6–10).

center of each particle using a single-point analysis technique. Particle-free areas of the glass were also measured using EDS to obtain a control spectrum from the coated glass substrate. While this single-point approach was more labor-intensive, it increased our ability to reduce noise and minimize spectral contamination from the glass substrate. Monte Carlo simulations conducted at 15 kV accelerating voltage showed that for particles smaller than 1.5 µm, some x-rays are emitted from the glass substrate, though this impact is minimized for particles down to 1 µm. To further ensure reliable results, we classified particles based on element identification rather than quantifying with weight percentage values, which helps account for potential variations in signal intensity across different regions of particles. Additional details on this process and considerations when choosing coating material and EDS analysis techniques are available in Bernal Ayala et al. (2024b).

2.1.2 Elemental characterization

A unique feature of this technique is its capacity to link the elemental composition along with the size of individual particles with their location and proximity to the hailstone embryo. Due to these particles' small size and complexity, EDS spectra were primarily used for element identification, focusing on the presence and relative abundance of key indicator elements to interpret particle identity. This approach was chosen instead of calculating quantitative elemental abundances from EDS measurements for several reasons.

First, the particles were covered by a ∼ 1 µm thick slightly varying layer of Formvar (a carbon-based material) and further coated with a 10 nm layer of either gold (Au) or a gold–palladium (Au–Pd) conductive coating. Additionally, the particles rested on a soda–lime glass substrate containing elements like silicon (Si), aluminum (Al), sodium (Na), calcium (Ca), potassium (K), and oxygen (O), which contributed to the X-ray signals. While we aimed for spectrum deconvolution to account for signatures from both the coating materials and the substrate (Bernal Ayala et al., 2024b), we recognize further complications introduced by slight spatial variations in Formvar thickness and thus relied on elemental presence and relative abundance rather than absolute quantitative abundances for our particle classification.

To further justify our classification approach, we note that analyzing particles with irregular geometries presents additional challenges in trying to quantify abundances (Fletcher, 2011; Goldstein et al., 2017). EDS is fundamentally designed for flat, homogeneous materials when applied to small, polyphase, or irregularly shaped particles. Complications arise due to assumptions in the matrix correction and irregularities in X-ray production, emission, and take-off angles to the detector that impact quantifying elemental abundances from the EDS spectrum. Additionally, the EDS spectrum represents all X-rays produced within an approximate 2–4 μm^3 activation volume at the beam's impact location. Given that many aerosol dust particles (as an example noted in Sect. 1) exhibit heterogeneity at the submicron scale, numerous EDS spectra will reflect polyphase materials.

For these reasons, we did not place high confidence in the absolute values of elemental weight percentages. Instead, EDS spectra were interpreted based on the presence of characteristic elements corresponding to specific mineral phases. More specifically, particles with high concentrations of carbon (C) and oxygen (O) were interpreted as organics, while others with a significant presence of nitrogen (N) were identified as nitrates. Lithic fragments were identified as pieces of eroded rock rich in Si, Al, Na, Ca, Mg, and Fe. Agglomerated carbon–lithic or carbon–lithic–clay fragments showed signatures rich in C, Si, Al, Na, Ca, Mg, and Fe, representing potential organic mixtures with dust and other particles in the region (referred to as agglomerated mineral/organics). An example of this agglomerated mineral/organics classification is shown in Fig. 4a, characterized by strong Si, Al, Na, Ca, and Mg peaks in its EDS spectrum. The addition of CLSM, which provides information about particle color and general morphology, and SEM's high-resolution surface imaging with the EDS's elemental analysis allows for particle classification that considers both chemical composition and physical structure. Here (Fig. 4a), the CLSM image reveals a bright, irregularly shaped particle against the dark background. In contrast, the corresponding SEM image shows its complex three-dimensional structure with multiple crystalline components, supporting its classification as an agglomerate.

The middle panel (Fig. 4b) demonstrates a Fe-rich organic particle with dominant O and Fe signals. The CLSM image shows a reddish-brown coloration characteristic of Fe-rich particles, while the SEM reveals a smooth, folded surface with sharp-edge structures. This spectral and morphological evidence combination supports its classification as a Fe-rich organic particle. The right panel (Fig. 4c) reveals a salt particle with prominent Cl and Na peaks, characteristic of halite. The CLSM image shows a dark, well-defined particle. In contrast, the SEM image displays an irregular shape with uneven edges and lacks the symmetrical, straight-edge characteristics typically associated with cubic morphology, such as those found in halites. This elemental classification scheme also identified distinct minerals including quartz and calcite. We also detected particles containing unique indicator elements, such as groups of zinc chloride, copper zinc chloride, or copper chloride particles, with EDS spectra rich in Zn–Cl, Zn–Cu–Cl, or Cu–Cl, respectively.

2.1.3 Air mass trajectories

The NOAA Air Resources Laboratory's Hybrid Single-Particle Lagrangian Integrated Trajectory model (HYSPLIT; Stein et al., 2015) was first used to generate a 24 h air mass back-trajectory using 0.28° × 0.28° European Environment Agency Reanalysis datasets (ERA5; Hersbach et al., 2020) with a vertical resolution of 37 pressure levels: 25 hPa intervals from 1025 to 750 hPa, 50 hPa intervals from 750 to 300 hPa, and 25 hPa intervals from 275 to 100 hPa. Trajectories were initiated at 17:00 UTC on 8 February and 22:00 UTC on 13–14 December, with hourly intervals starting at heights of 100, 500, 1000, and 1500 m a.g.l. (above ground level) from convective core coordinates on 8 February (64.75° W, 31.59° S, marked by a red star in Fig. 1) and on 13–14 December (64.45° W, 32.20° S; marked by a blue star in Fig. 1). These initiation coordinates were identified using channel 11 (8.4 µm) from the geostationary satellite GOES-16 (Bernal Ayala et al., 2022).

These initiation height levels were chosen for the following reasons: 100 m is the lowest point to the surface and the first pressure level, 500 and 1000 m provide boundary layer variability, and 1500 m focuses on possible particle transport influences from the low-level jet (Bernal Ayala et al., 2024b; Sasaki et al., 2024). A trajectory matrix with a 7 × 5 grid and 0.30° spacing was also processed from the initial convective pixel coordinate at 17:00 and 22:00 UTC (on 8 February and 13–14 December, respectively) for 5 d to better understand which local and longer-range sources could have transported particles at the initiation location before hail-producing convection was observed. The area covered by all back-trajectories resulting from the matrix was divided into grid cells with dimensions of 0.28° longitude and 0.28° latitude (i.e., ERA-5 horizontal resolution). Each trajectory occurrence in each grid cell was then normalized based on the time spent over each grid cell and included trajectory endpoints for all the heights (ERA5; Ashbaugh et al., 1985). Residence-time coefficient pixels were overlaid on the C3S Land Cover classification gridded map from 2023, as shown in Fig. 1. This map provides a global description of the land surface divided into 22 classes, available through the C3S Climate Data Store and defined using the United Nations Food and Agriculture Organization's Land Cover Classifica-

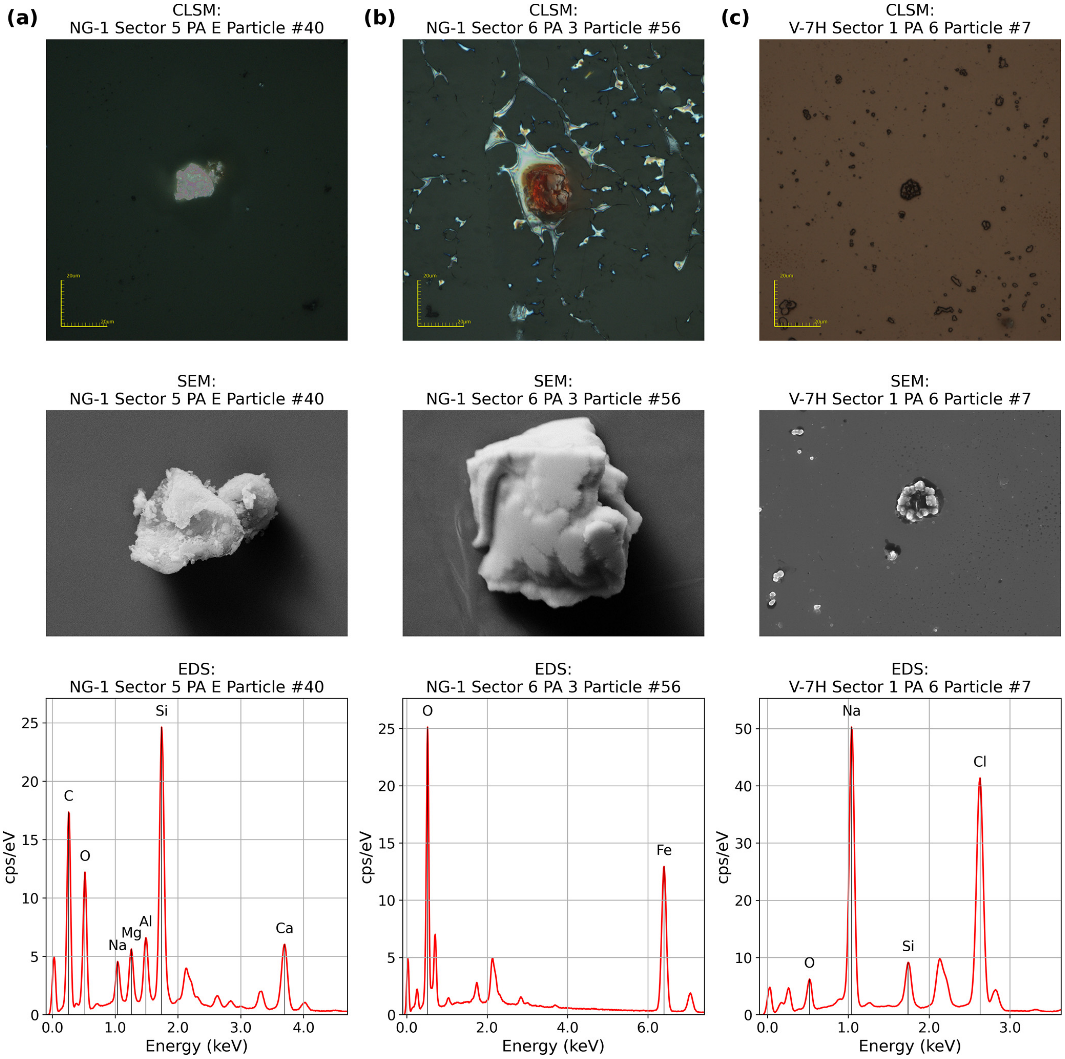

Figure 4. Examples of particles analyzed using three complementary techniques: confocal laser scanning microscopy (CLSM; top row), scanning electron microscopy (SEM; middle row), and energy-dispersive X-ray spectroscopy (EDS; bottom row). Column **(a)** shows an agglomerated mineral/organic particle. Column **(b)** displays a Fe-rich organic particle. Column **(c)** shows a salt particle from V-7H Sector 1, with prominent Na and Cl peaks characteristic of halite. The CLSM images provide optical characteristics and context within the hailstone, while SEM reveals detailed surface morphology, and EDS spectra confirm elemental composition. Scale bars in CLSM images represent 20 µm.

tion (Copernicus Climate Change Service, 2019). This approach provides insight into the highest probability of specific land-use regions being possible source regions for the non-soluble particulates analyzed in this study.

3 Results

3.1 8 February 2018

On 8 February 2018, an isolated supercellular convective system developed east of the Sierras Grandes, located in the northern section of the SDC (lime green star; Fig. 1). This convective system produced record-breaking gargantuan hail (Kumjian et al., 2020) in Villa Carlos Paz, in addition to the 4 cm hailstone collected and analyzed in this study (V-7). While a warm, humid, conditionally unstable air mass was present, supporting the initiation and growth of deep convection on this day (Kumjian et al., 2020), with a large-scale pattern similar to composites for supercell environments in this region (Mulholland et al., 2018), a northerly low-level jet, often linked to large-scale moisture transport (e.g., Sasaki et al., 2024) and deep, widespread convective systems in this region (e.g., Rasmussen and Houze, 2016), was lacking during this case. This particular hail-producing storm, therefore, developed under more local influences, including strong upslope flow along the SDC (Bernal Ayala et al., 2022), that

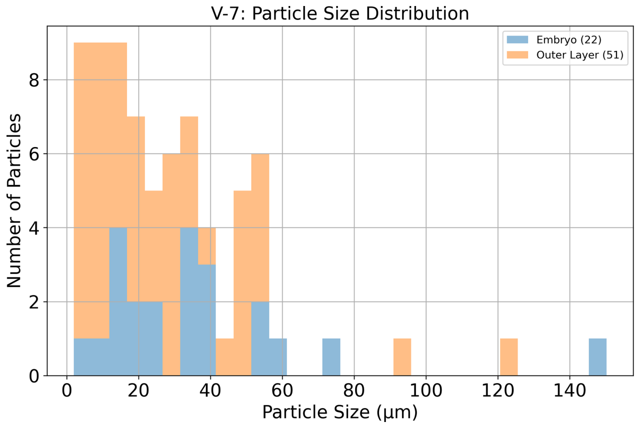

Figure 5. Particle size distribution (in µm) through the V-7 cross-section is shown in Fig. 2, where the particle size distribution in the hailstone embryo region is represented by blue pastel bars, and the particle size distribution in the outer layers of the hailstone is shown by orange pastel bars.

are likely to affect potential source regions of particles found within the V-7 hailstone from this case.

3.1.1 Particle size and elemental composition of individual particles

This V-7 hailstone analyzed in this case included particles analyzed in both the embryo and the outer layers through a vertical cross-section of the 4 cm stone (Fig. 2). The CLSM analysis of V-7 revealed particle sizes ranging from 2 to 150 µm (Fig. 5), with an average particle size of 30 µm. This indicates that particle sizes vary, with many particles being much smaller or larger than the average particle size. The minimum size measured was 2 µm, close to the minimum observable particle size using this method (1 µm; Bernal Ayala et al., 2024b). When focusing on particles within the embryo (22 particles), sizes ranged from 6 to 150 µm. In contrast, the particles we sampled in the outer layers (51 particles) were smaller over a narrower range, encompassing sizes from 2 to 122 µm. While the comparison between the embryo and outer layers in V-7 suggests that the embryo contained larger particles than the outer layers, a key point here is that both regions contained particles exceeding 100 µm.

With a large range of particle sizes identified in the hailstone, the elemental classification scheme described in Sect. 2.3 was applied to this hailstone sample to determine the compositions of these individual particles. Overall, the particles in V-7 were primarily characterized as agglomerated minerals/organics (∼ 41 %; Fig. 6a; Table 1) and distributed throughout the hailstone (Fig. 7). The particle sizes in this category ranged from 6 to 75 µm in the embryo (9 particles) and 2 to 55 µm in the outer layers (21 particles).

The second most prevalent group was agglomerated salts (∼ 16 %; Fig. 6a; Table 1), characterized by strong Cl and Na signals in EDS analysis and distributed throughout the hailstone (Fig. 7). The 10 particles in this category analyzed in the outer layers ranged from 5 to 122 µm in the outer layers. Of the 2 particles of this type sampled in the embryo, one was 13 µm, while the other was the largest particle recorded in this group and in the entire V-7 sample at 150 µm. Interestingly, even though this large particle was identified as a salt, it did not support a large single crystal but an agglomeration of smaller crystals (not shown). Instead, this particle exhibited a strong carbon peak, indicating a small salt particle atop a potential agglomerated mineral/organic particle.

At 8 % frequency, Zn–Cl-rich particles (Fig. 6a; Table 1) consisted of Zn–Cl content greater than 1 % by weight. A single particle of 33 µm was found in the embryo, while particles in the outer layers ranged from 7 to 25 µm (5 particles; Fig. 7). Organic particles (∼ 8 %; Fig. 6a; Table 1), containing more than 60 % weight of carbon and rich in oxygen, were found in both regions with sizes ranging from 22 to 33 µm in the embryo and 10 to 23 µm in the outer layers, with 3 particles in both regions (Fig. 7). Similarly, at 8 % frequency, clays (Fig. 6a; Table 1), characterized by high aluminum content and the presence of Si, K, Ca, Na, Mg, and Fe, were composed of 2 particles in the embryo of sizes 20 and 55 µm and 4 particles analyzed in the outer layers ranging from 4 to 47 µm.

Shifting to the larger-than-average particle sizes found in V-7 are quartz particles (∼ 7 %; Fig. 6a; Table 1), identified as silicon content greater than 30 % by weight, with 2 particles analyzed in the embryo of sizes 16 and 22 µm and 3 in the outer layers ranging 38 to 55 µm in size. Ammonia/nitrate particles (∼ 7 %; Fig. 6a; Table 1), which were nitrogen-rich with content greater than 7 % by weight, included 3 particles in the embryo ranging in size from 37 to 58 µm and 2 in the outer layers (31 and 45 µm). Two Fe-oxide particles (∼ 3 %; Fig. 6a; Table 1), dominated by iron and oxygen with no carbon or silicon, were located in the outer layers of the hailstone with sizes of 33 and 92 µm (Fig. 7). Although Fe oxides were only detected in the outer layers in this particular swath, a second swath conducted in a different direction across the hailstone (not shown) identified Fe-oxide particles in the embryo as well. This trend for all particle categories to be found throughout the whole sample extended to the final identified category, lithics (1 %; Fig. 6a; Table 1), characterized by a silicon content of 20 %–40 % weight, along with high concentrations of Na, Mg, and Ca; minor amounts of Al and K; and no detectable carbon from the Formvar. Only one particle, measuring 5 µm, was identified in this category and located in the hailstone sample's outer layer (Fig. 7); however, the second swath (not shown) revealed additional lithic particles within the embryo.

By analyzing the elemental composition of individual particles within the hailstone, the dominance of large, agglomerated particles (including those with salt) in the sample suggests a link to local land use, including hypothesized agricultural and biological sources. While particles of up to 100 µm

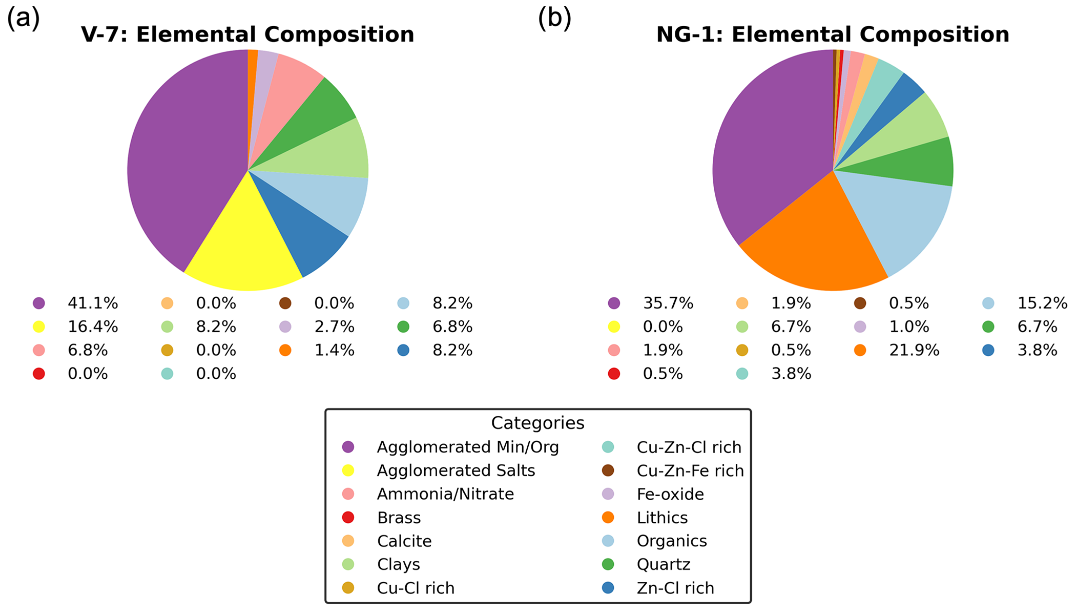

Figure 6. Elemental composition distributions for particles selected within the 2-D cross sections for **(a)** V-7 and **(b)** NG-1.

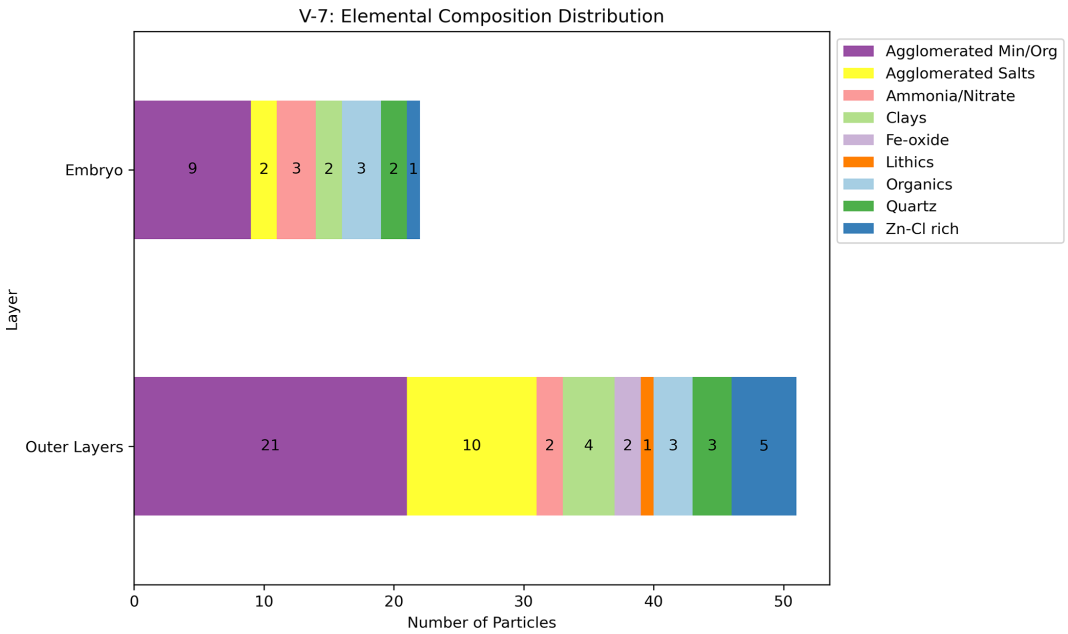

Figure 7. Elemental composition distribution for particles identified in the V-7 cross-section shown in Fig. 2.

are likely to remain suspended in the atmosphere for up to 2 d (Jaenicke, 1978; Bakan et al., 1987), the largest of the particles observed within the V-7 hailstone (i.e., 150 µm agglomerated salt in the embryo) were likely ingested into the storm from local sources near the SDC. The HYSPLIT back-trajectory analysis provides further insight into these links.

3.1.2 Possible source regions

The analysis of the 24 h HYSPLIT back-trajectory (Fig. 8a) provides information on the possible origins of the particles in the V-7 hailstone sample with distinct patterns at different altitude levels. Levels 100 and 500 m a.g.l. show trajectories near the initiation point from the northwest but earlier in the 24 h period had curved over the northeastern part of the SDC, likely owing to the upslope flow of surface winds from the northeast (Bernal Ayala et al., 2022). This ups-

Table 1. Particle size ranges for each elemental category identified in hailstone samples V-7 and NG-1, separated by location within the hailstone (embryo versus outer layers).

Category	Particle size range (µm)			
	V-7		NG-1	
	Embryo	Outer layers	Embryo	Outer layers
Agglomerated Min/Org	6–75	2–55	4–77	9–109
Ammonia/nitrate	37–58	31, 45	No particles	23–36
Brass	No particles	No particles	No particles	1
Calcite	No particles	No particles	12, 24	8, 13
Clays	20, 55	4–47	10–62	3–69
Cu–Cl-rich	No particles	No particles	No particles	32
Cu–Zn–Cl-rich	No particles	No particles	No particles	6–78
Fe oxide	No particles	33, 92	21	61
Lithics	No particles	5	5–58	8–181
Organics	22–33	10–23	9–256	13–216
Quartz	16, 22	38–55	12–81	20–64
Agglomerated salts	13, 150	5–122	No particles	No particles
Zn–Cl-rich	33	7–25	9–34	3
Cu–Zn–Fe-rich	No particles	No particles	No particles	27

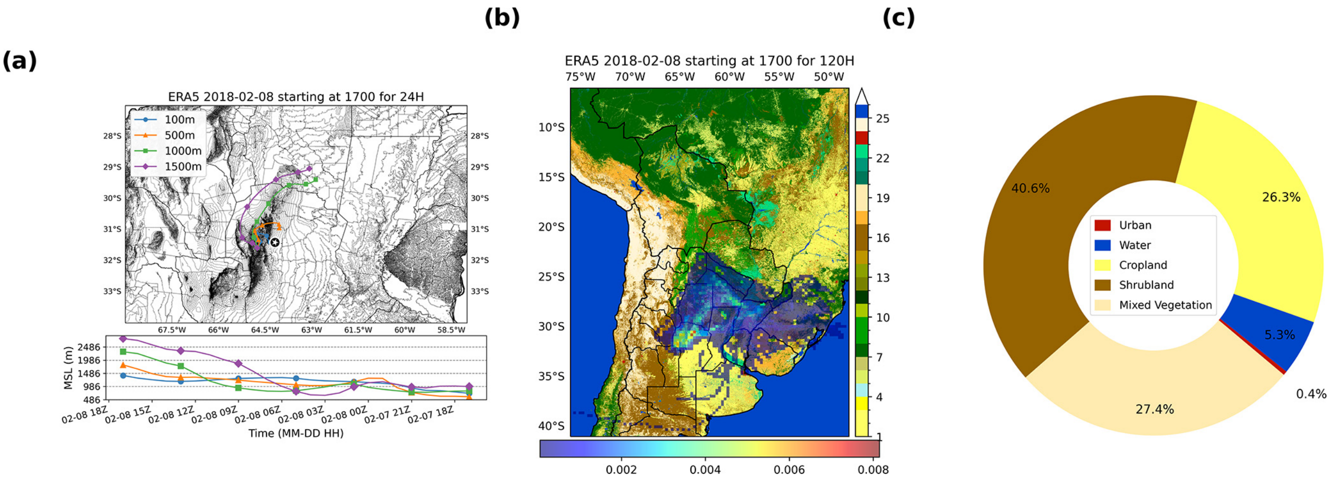

Figure 8. HYSPLIT analysis for 8 February 2018. Panel **(a)** (top) shows 24 h HYSPLIT back-trajectories color-coded by height (in meters), with Córdoba marked by a white star. The bottom of **(a)** displays terrain analysis in meters above sea level for the same time periods as the back-trajectories. Panel **(b)** shows residence-time coefficients calculated for 5 d back-trajectories overlaid on the C3S Land Cover map with the city of Córdoba marked by a white star. The land cover colors correspond to a subset of categories shown in Fig. 1, specifically as follows: 1/2/3 – Cropland rain-fed, 4 – Cropland irrigated, 5 – Mosaic cropland, 6 – Mosaic natural vegetation, 7 – Evergreen broadleaved, 8/9/10 – Deciduous broadleaved, 11 – Evergreen needle-leaved, 12 – Mixed trees, 13 – Mosaic tree/shrub, 14 – Mosaic herbaceous, 15/16 – Shrubland, 17 – Grassland, 18 – Sparse vegetation, 19 – Sparse herbaceous, 20 – Fresh water flooded tree cover, 21 – Saline water flooded tree cover, 22 – Flooded shrub/herbaceous cover, 23 – Urban, 24 – Bare areas, 25 – Water, 26 – Snow and ice. Panel **(c)** displays the predominant land uses within the residence-time coefficient pixels observed in **(b)**. Similar land uses were grouped into the following categories: Urban (23), Water (25, 26), Cropland (1, 2, 3, 4, 5), Shrubland (15, 16, 17), and Mixed Vegetation (6, 7, 8, 9, 10, 11, 12, 13, 14, 18, 19). Flooded Vegetation (20, 21, 22) and bare areas (24) were not included.

lope flow is supported by the terrain and height change of the trajectory seen in Fig. 8a (bottom figure). The 1000 and 1500 m a.g.l. trajectories came from the north and northwest near the initiation point but, moving back in time, showed a slight curvature north and northeast of the Cordoba Province at distances farther than the lower levels. Within this short time frame, the SDC will likely impact the particle sources found in the hailstone. However, longer-range transport of particles prior to 24 h may also have deposited particles in the area that could have been ingested into the 8 February supercell.

To investigate potential source areas further back in time, the residence-time coefficients calculated for the 5 d back-trajectory matrices (Fig. 8b) similarly highlight the regional influence indicated in the 24 h trajectories in that most trajectories lie within the Argentinian borders. More specifically, under the assumption that the particles arriving at the location where the hail-producing storm initiated are more likely emitted from regions where the air masses spent more time (Yadav et al., 2021; Ren et al., 2021; Testa et al., 2021), the grid cells showing the high-residence-time coefficients (any grid that includes more than one HYSPLIT trajectory) are considered potentially principal sources for the particles found in the hailstone. The regions with the highest-residence-time coefficients for 5 d leading up to the V-7 storm initiation (orange, yellow, and red in Fig. 8b) are generally located over the SDC, city of Córdoba (white star in Figs. 1 and 8b); Argentina's largest natural salt lake (Laguna Mar Chiquita; 30.71° S, 62.56° W); and provinces such as Santiago del Estero, Chaco, Santa Fe, and Corrientes (see Fig. 1 as a geographical reference). These results reveal that sources within Argentina's geographical limits account for possible non-soluble particle sources in the analyzed hailstone sample. More specifically, in comparing the high-residence-time coefficient pixels from the 5 d back-trajectory with the C3S Land Cover map (Fig. 8b), we find the most predominant land uses (Fig. 8c) corresponding to shrublands, croplands, mixed vegetation, urban areas (mostly the city of Córdoba), and areas with a body of water (including the aforementioned salt lake), consistent with the imprints of soil dust, organics, salt, and minerals found throughout the V-7 hailstone, including the embryo, and emphasizing the importance of local land use on INP sources of hail formation.

3.2 13–14 December 2018

It is not uncommon for hail-producing storms in Argentina to form from larger convective systems in environments characterized by air transport from non-local sources (e.g., Rasmussen and Houze, 2016; Sasaki et al., 2022, 2024). Therefore, it is worthwhile to compare the V-7 hailstone with one collected in this type of environment to explore potential non-local sources on hail formation. The 8 cm NG-1 hailstone collected during the 13–14 December 2018 event was associated with a mesoscale convective system (MCS) that developed in the southern portion of the SDC (blue star; Fig. 1). In contrast to the 8 February supercell case, this hail-producing MCS was associated with increased moisture from the South American Low-Level Jet (SALLJ), dry-air subsidence east of the Andes capping the low-level moist layer, and lee cyclogenesis resulting from the passage of an upper-level trough (Bernal Ayala et al., 2022; Sasaki et al., 2022), all characteristics of environments favorable for MCSs in this region (Rasmussen and Houze, 2016; Mulholland et al., 2018; Bruick et al., 2019; Sasaki et al., 2024). As such, particularly owing to the SALLJ's large-scale transport of air and likely associated particles from a farther distance, the hypothesis was that there would be different particle compositions in this stone compared to the 4 cm stone of 8 February (a supercell dominated by more local influences including strong upslope flow).

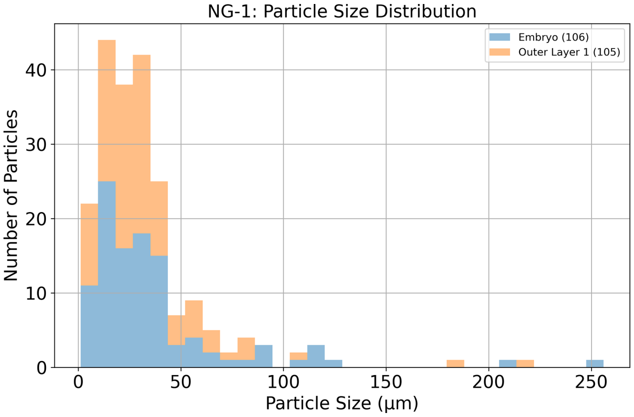

Figure 9. Particle size distribution (in µm) through the NG-1 cross-section is shown in Fig. 3, where the particle size distribution in the hailstone embryo region is represented by blue pastel bars, and the particle size distribution in the outer layers of the hailstone is shown by orange pastel bars.

3.2.1 Particle size and elemental composition of individual particles

For NG-1, particle size ranged from 1 to 256 µm (Fig. 9), with an average particle size of 35 µm. The largest particle in NG-1 was ∼ 100 µm larger than the largest in V-7, and the average particle size was also larger in NG-1 (35 µm) compared to V-7 (30 µm). This shows that both hailstones' particle sizes had large variations. When focusing on particles within the embryo (106 particles) and the outer layers (105 particles), large particles (i.e., > 100 µm) were found throughout the hailstone, with large size variability observed in both regions. Like V-7, the elemental classification scheme applied to NG-1 showed that the particles were primarily composed of agglomerated minerals/organics (∼ 36 %; Fig. 6b; Table 1), with sizes ranging from 4 to 77 µm in the embryo (33 particles) and 9 to 109 µm in the outer layers (42 particles) and were similarly found throughout the NG-1 hailstone sample (Fig. 10).

While one relatively small lithic particle was identified in V-7 (Table 1, Fig. 6), lithics were the second most prevalent group in NG-1 (∼ 22 %; Fig. 6b; Table 1), with particle sizes ranging from 5 to 58 µm in the embryo (26 particles) and 8 to 181 µm in the outer layers (20 particles; Table 1), and were distributed throughout the hailstone, with 26 particles in the embryo and 20 in the outer layers (Fig. 10). Organic particles

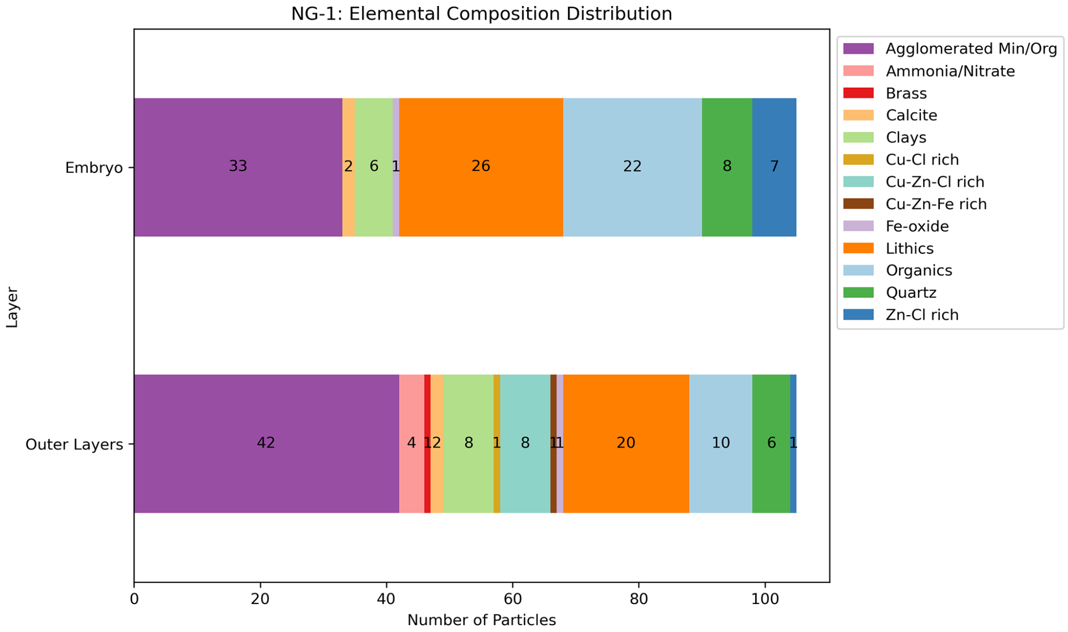

Figure 10. Elemental composition distribution for particles identified in the NG-1 cross-section shown in Fig. 3.

were also more prevalent in NG-1 (∼ 15 %; Fig. 6b; Table 1) than in V-7 (∼ 8 %; Fig. 6a; Table 1). This category contained the largest particle size found in NG-1, ranging from 9 to 256 µm in the embryo (22 particles) and 13 to 216 µm in the outer layers (10 particles), also distributed throughout the hailstone (Fig. 10). Similar to V-7, quartz particles were found throughout the hailstone (Fig. 10), with sizes ranging from 10 to 62 µm in the embryo (8 particles) and 3 to 69 µm in the outer layers (6 particles; Table 1). While less prevalent, ammonia/nitrate particles were also detected in NG-1, ranging from 23 to 36 µm, and found exclusively in the outer layers with 4 particles (Fig. 10; Table 1).

Despite the consistency in particle elemental categories found within both hailstones, some categories were unique to NG-1. Cu–Zn–Cl-rich particles (∼ 4 %; Fig. 6b; Table 1), with particle sizes ranging from 6 to 78 µm, were exclusively located in the outer layers with 8 particles (Fig. 10). A single Cu–Cl-rich particle (∼ 1 %; Fig. 6b; Table 1) measuring 32 µm was found in the outer layers (Fig. 10). Calcite particles (∼ 2 %; Fig. 6b; Table 1) showed size ranges of 12 and 24 µm in the embryo and 8 and 13 µm in the outer layers, with 2 particles in each region (Fig. 10). Finally, a single brass particle (∼ 1 %; Fig. 6b; Table 1) measuring 1 µm, characterized by strong Cu and Zn signals in EDS analysis, was found in the outer layers (Fig. 10).

Overall, while both hailstone samples showed similarities in certain categories such as quartz, nitrate particles, and Fe oxides (with NG-1 showing particles of 21 µm in the embryo and 61 µm in the outer layers), there were notable differences in the presence and distribution of lithics, organics, Cu–Zn–Cl-rich, Cu–Cl-rich particles, brass, and calcite, as well as the presence of salts in V-7 but their absence in NG-1. Were these different particle compositions linked to different trajectories associated with these different storms, including more non-local sources on 13–14 December? To explore this question, the HYSPLIT trajectories are again analyzed for the 24 h and 5 d time frames.

3.2.2 Possible source regions

The 24 h HYSPLIT back-trajectory analysis was applied to the 13–14 December case (Fig. 11a) to determine potential source regions of the particles found within the NG-1 hailstone sample. Nearest the initiation point, the trajectories originate from the west and northwest at all analyzed levels. In particular, trajectories curved around the northern section of the SDC, moving upslope along the western side of the southern section of SDC instead of the eastern side as on 8 February. The 1500 m a.g.l. levels followed a similar path to that of the lower-level winds but started at regions farther north than the lower trajectories. This trajectory height and the direction are likely linked to the SALLJ and thus could have led to more remote sources of particles over a longer time period.

Therefore, residence-time coefficients for 5 d back-trajectories matrices were again calculated (Fig. 11b) to explore potential sources outside of Argentina's geographical limits. Unlike on 8 February, when the trajectories were primarily within Argentinian territories, on 13–14 December, air mass trajectories with high residence times also came from Paraguay and Brazil. Under the same aforementioned assumption that the particles arriving at the location where the hail-producing storm initiated are more likely emitted

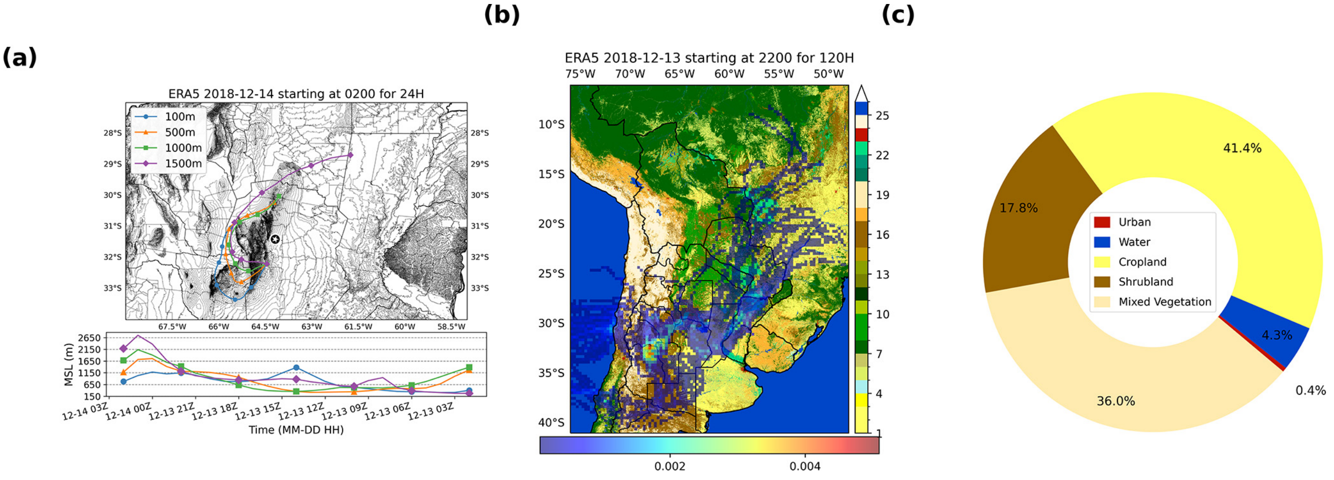

Figure 11. HYSPLIT analysis for 13-14 December 2018. Panel **(a)** (top) shows 24 h HYSPLIT back-trajectories color-coded by height (in meters), with the city of Córdoba marked by a white star. The bottom of **(a)** displays terrain analysis in meters above sea level for the same time periods as the back-trajectories. Panel **(b)** shows residence-time coefficients calculated for 5 d back-trajectories overlaid on the C3S Land Cover map with Córdoba marked by a white star. The land cover colors correspond to a subset of categories shown in Fig. 1, specifically as follows: 1/2/3 – Cropland rain-fed, 4 – Cropland irrigated, 5 – Mosaic cropland, 6 – Mosaic natural vegetation, 7 – Evergreen broadleaved, 8/9/10 – Deciduous broadleaved, 11 – Evergreen needle-leaved, 12 – Mixed trees, 13 – Mosaic tree/shrub, 14 – Mosaic herbaceous, 15/16 – Shrubland, 17 – Grassland, 18 – Sparse vegetation, 19 – Sparse herbaceous, 20 – Fresh water flooded tree cover, 21 – Saline water flooded tree cover, 22 – Flooded shrub/herbaceous cover, 23 – Urban, 24 – Bare areas, 25 – Water, 26 – Snow and ice. Panel **(c)** displays the predominant land uses within the residence-time coefficient pixels observed in **(b)**. Similar land uses were grouped into the following categories: Urban (23), Water (25, 26), Cropland(1, 2, 3, 4, 5), Shrubland (15, 16, 17), and Mixed Vegetation (6, 7, 8, 9, 10, 11, 12, 13, 14, 18, 19). Flooded Vegetation (20, 21, 22) and bare areas (24) were not included.

from regions where the air masses spent more time, the regions with the highest-residence-time coefficients (orange, yellow, red, and lighter shades of blue in Fig. 11b) were generally located northwest of the SDCs, in the boundary between Cordoba, the southwestern corner of La Rioja and San Luis provinces (Fig. 1), and in locations outside of Argentina. While the main land-use categories associated with the highest residence times are generally the same for both cases (i.e., Figs. 8c and 11c), the distribution shifts on 13–14 December from pixels associated with shrublands to more pixels associated with both cropland and mixed vegetation (Fig. 11b). The dominance of the cropland category again is consistent with the prevalence of agglomerated mineral/organics, but the trajectories from either the west side of the SDC or the regions north of Argentina could explain unique source regions to NG-1 resulting in particle elemental compositions not observed or more prevalent than in V-7 (e.g., lithics, Cu–Zn–Cl-rich, Cu–Cl-rich, brass, calcite). There were also low-residence-time pixels over the salt lake (Fig. 11b), potentially explaining why no salt was found in NG-1.

4 Discussion

Our study presents the first analysis of the sizes, composition, and distribution of non-soluble particles in hailstones from storms in Argentina. Unlike previous studies that melted hailstones to evaluate their overall composition (Šantl-Temkiv et al., 2013; Michaud et al., 2014; Beal et al., 2021), our approach (Bernal Ayala et al., 2024b) preserves both the non-soluble particles and their in situ locations within the hailstones. It uniquely allows for analysis of the elemental composition of individual particles, revealing elemental combinations that impact the ice nucleating ability of those particles.

Applying our method to two hailstone cases from different storm modes in central Argentina revealed that the majority of particles in both hailstones are agglomerated minerals/organics, found both within the embryo and throughout the outer layers of the hailstones and exceeding 100 µm in size. The largest particle (256 µm in NG-1) was identified in the embryo with a relative abundance of carbon and oxygen. This relative composition abundance is consistent with the presence of organic particles identified in hailstones in China (Zhang et al., 2023), where they used SEM-EDS and machine learning to analyze non-soluble particles through a melting and filtering technique. However, our unique approach, which enables the analysis of individual particles, suggests that particle agglomeration in particular may have played a significant role in hail formation within our central Argentina cases, whether through physical coagulation in turbulent updrafts, water-mediated aggregation in mixed-phase regions, or surface modification through chemical coating (Wang et al., 2024; Michaud et al., 2014; Mokkapati, 2009). Indeed, with a link to cropland through our particle trajectory analysis and prior studies emphasizing the role of coated and aggregated mineral dust in ice nucleation (e.g., Steinke et al., 2016; Iturri et al., 2017; Cornwell et al., 2024), this work supports that agglomerated mineral dust particles, modified through atmospheric aging and coating processes, likely serve as efficient INPs for hail formation.

The breakdown of particle sizes by type and location in Table 1 reveals several insights. First, while both hailstones contained agglomerated mineral/organic particles throughout, their size distributions differed between embryo and outer layers, with NG-1 showing larger sizes in outer layers (up to 109 µm) compared to V-7 (up to 55 µm). Second, certain particle types showed distinct location preferences; for instance, Cu–Zn–Cl-rich and Cu–Cl-rich particles were found in NG-1's outer layers, while agglomerated salts were present throughout V-7 but entirely absent in NG-1. These spatial patterns provide information about particle availability during different stages of hail formation. Third, while the largest particles in both hailstones were found in their respective embryos, their compositions differed markedly: an organic-rich particle (256 µm) in NG-1 versus an agglomerated salt particle (150 µm) in V-7. This compositional difference in the embryonic particles suggests distinct aerosol populations were available during initial ice formation in these different storm types, potentially serving as INPs and thus providing information about the types and sizes of particles available for ice nucleation in these storms (Pruppacher and Klett, 1980; Heymsfield and Pflaum, 1985). In contrast, particles found in the outer layers were likely collected during the hailstone's growth process, becoming trapped within each successive layer as the hailstone grew through various cloud regions (Rangno and Hobbs, 1991). This distinction allows our study to simultaneously characterize both the potential INP population present during hail initiation and the broader array of particles encountered during hailstone growth and development through the cloud.

Beyond the particle-specific characteristics revealed by our analysis method, our findings demonstrate broader connections to regional characteristics that align with previous studies. Similar relationships between hailstone composition and regional soil signatures have been observed in hailstones collected in Slovenia and the triple-border region of Paraná, Brazil, and Argentina (Šantl-Temkiv et al., 2013; Beal et al., 2021), expanding beyond agricultural activities to other influences of local land cover. Their results are consistent with our findings that quartz, clays, and agglomerated mineral/organic particles were abundant in our hailstones, particularly associated with the highest residence times of trajectories over and near the SDC. These particle trajectories also showed a link to a nearby salt lake (Laguna Mar Chiquita) on 8 February, where the largest particle in V-7 was categorized as an agglomerate that contained salt. A recent modeling study of this lake emphasized that it is one of many that are shrinking, exposing dry lake beds that present a source of Na-rich mineral dust (Borda et al., 2022). The presence of this large mineral–organic agglomerate with salt in the hailstone embryo and the potential link back to this shrinking salt lake emphasize another anthropogenic source of potential INPs or non-soluble cloud condensation nuclei (CCN) to consider in hail formation and growth.

This anthropogenic link is also suggested through elemental composition results from the NG-1 hailstone, particularly through the presence of Cu–Zn–Cl-rich (4 %) and Cu–Cl-rich (1 %) particles that were not observed in V-7. The trajectory analysis for NG-1 showed sources both within and outside Argentina under the general "croplands" category, suggesting these particles may originate from agricultural activities over a broader region. Specifically, the presence of Cu–Cl compounds suggests a potential link to agrochemicals like copper chloride, commonly used for pest control (Lewis et al., 2016). According to a market report, copper oxychloride is used globally as a fungicide for crop protection, including in Argentina (Manoj, 2023). While natural sources cannot be ruled out, international databases (e.g., https://www.mindat.org/, last access: 18 October 2024) reveal several Cu–Cl evaporite minerals actively mined in the Chilean Atacama Desert, the correlation with cropland trajectories and agricultural regions supports an agrochemical origin for these particles.

Zinc-containing particles in both hailstones (Zn–Cl-rich in V-7 at 8 % frequency; Cu–Zn–Cl-rich at 4 % in NG-1) suggest consistent regional sources of zinc aerosols. While zinc is typically not found in significant atmospheric concentrations, several regional sources could explain its presence in our samples. Argentina's significant zinc production, particularly from the Aguilar Mine in Jujuy Province, which produced over 23 000 t of zinc in 2017 (USGS, 2019; International Trade Administration, 2023), represents a potential source. Additionally, the agricultural sector's use of zinc-based fertilizers (e.g., ZINC 700 and Status ZN) for seed treatment in crops like fruit trees, vineyards, vegetables, rice, corn, and wheat (Argentina, 2024; Rizobacter, 2024) aligns with our trajectory analysis over croplands. Natural sources may also contribute, as ecandrewsite (ZnTiO3) and other ilmenite-group minerals have been identified in amphibolites from the SDC basement Espeche and Lira (2022).

The Fe-oxide particles identified in both hailstones, while less prevalent (3 % in V-7), likely originate from three potential sources in the region: natural processes, agricultural activities, and anthropogenic factors. The SDC range contributes through weathering and erosion of iron-rich formations, including metamorphosed iron ore in the Sierra de Comechingones containing magnetite, hematite, goethite, limonite, and siderite (Zaccarini et al., 2004). Agricultural areas around Córdoba may also contribute through naturally iron-rich soils and the use of iron-containing fertilizers (e.g., Caburé, 2024; SRL, 2021). These Fe-oxide particles throughout both hailstones and their relatively large sizes (33–92 µm in V-7) suggest efficient transport and incorporation mechanisms during hail formation.

Understanding the origins of these minerals highlights the environmental impact of human activities, such as agricultural practices, and the natural contributions from surrounding geological features, like the SDC, on aerosol sources, including those involved in hail formation and growth. The presence of large agglomerated particles (> 100 µm) in both hailstones, particularly in their embryos, suggests that these particles play a crucial role in hail initiation. Their composition, ranging from mineral–organic mixtures to metal-rich compounds, reflects the region's natural and anthropogenic sources. This study's findings emphasize the need to further explore aerosol sources' effects on hailstone growth and development with a global mindset to improve near- and long-term forecasting of these impacts.

5 Conclusions

Using a novel hailstone-analysis technique (Bernal Ayala et al., 2024b), this study provides first-of-its-kind insights into the size distribution, composition, and potential sources of non-soluble particles within hailstones from South America. Unlike traditional melting methods, our approach uniquely preserves the spatial distribution of particles within hailstones, allowing us to analyze both potential INPs in the embryo and particles collected during growth in the outer layers. These hailstones were collected in central Argentina from different storm modes under various environmental conditions, offering an opportunity to investigate potential variability in particle source regions and characteristics within hailstones that could influence their formation and growth. Through this unique approach, we found the following:

- Analyzed particles ranged in size from 1 to 256 µm, with the largest particles in each hailstone found in its embryo and larger particle sizes for the larger of the two hailstones. While our method's minimum observable size of 1 µm means we cannot detect smaller particles that may serve as INPs, particularly at colder temperatures, our ability to analyze larger particles (> 10 µm) provides crucial insights into a size range often excluded from traditional INP studies.
- Agglomerated mineral/organic particles dominated both hailstones' elemental composition, with an organic-rich particle being the largest (256 µm in NG-1 embryo), and were observed in all layers throughout the hailstones.
- Lithics and other particle types were found throughout both hailstones. The presence of similar particle characteristics in both embryos and outer layers provides valuable information about particle availability during both initiation and growth phases that would be lost in traditional melting methods.
- Contributions from agricultural practices and geological features were linked to hailstone formation. Both hailstones were associated with various regional land-use types, including shrublands, mixed vegetation, croplands, and urban areas. The particles found contained regional soil signatures, potentially influenced by agrochemicals used in pest control practices or crop fertilizers, as well as sodium-rich mineral dust from nearby dry lake beds.

These findings enhance our understanding of the interplay between atmospheric particle sources, both natural and anthropogenic, and their role in hailstone formation by linking the composition of particles within the hailstone embryo to local and regional land use. The value of our method lies not just in comparing embryo and outer layer compositions but in providing unprecedented spatial resolution of particle distributions throughout the hailstone. This preservation of spatial relationships enables several key insights impossible with traditional melting techniques: (1) evidence that large particles (> 100 µm) are present in embryos, challenging assumptions about size limitations in hail initiation; (2) characterization of particle size spectra across different regions; and (3) detailed analysis of individual particle characteristics in their original context.

The relationship between particle size and its ability to serve as an INP is complex and depends on multiple factors, including temperature, composition, and surface properties. While smaller particles (< 1 µm) can dominate ice nucleation at colder temperatures, larger particles (> 10 µm) generally exhibit higher ice-nucleating efficiency per unit mass because they provide greater surface area and can host diverse mineral or organic phases that promote ice formation (Kanji et al., 2017; Knopf et al., 2018). This aligns with our findings of large particles in hailstone embryos, representing the population of particles available during initial ice nucleation. In contrast, particles in outer layers were likely collected during subsequent growth phases.

The predominance of large particles in hailstone embryos has significant implications for understanding hail formation. These coarse particles likely remained suspended for extended periods in convective updrafts due to turbulent mixing, allowing them to aggregate with smaller aerosols and form composite INPs with enhanced nucleation activity (Testa et al., 2021). While our method suggests the role of large particles in hail embryo formation, integrating complementary techniques to detect submicron INPs would provide a more comprehensive understanding of the full spectrum of ice-nucleating processes. The similarities observed between the two hailstones studied suggest that the composition and size of aerosols, key inputs in hail formation and growth models, are crucial for accurate simulations. However, the larger NG-1 hailstone displayed a greater diversity and number of particles, indicating potential differences in particle accumulation and transport processes, likely influenced by varying storm modes.

This study contributes to ongoing hail research and highlights the potential impact of natural and human activities on hail growth. One technical limitation of our approach includes challenges in carbon characterization using EDS. Carbon contamination within the SEM chambers can result in low-level carbon detection across all EDS spectra. Moreover, EDS is less sensitive to light elements such as C. Our analysis confirmed that the contribution of carbon from the micrometer Formvar coating is minimal, as demonstrated through comparison of potential carbon signals in clear glass sections with and without Formvar (Bernal Ayala et al., 2024b). Additionally, while the glass substrate elements (Si, Al, Na, Ca, K, O) contribute to X-ray signals, our spectrum deconvolution approach allows us to account for these contributions in our particle classification. However, the EDS detector cannot differentiate the bonding environment of the carbon, making it impossible to determine if the carbon originates from inorganic sources (e.g., graphite), organic matter (e.g., detritus or pollen), or industrial materials (e.g., soot).

Despite these limitations, the techniques used in our research provide valuable insights into hail formation processes that complement existing methods. Similar particle characteristics in both stones suggest that initial conditions for ice nucleation may persist throughout the growth process, a finding only possible through spatial preservation. Future studies can apply this technique to hailstone samples from different regions globally to investigate whether similar particle characteristics are observed elsewhere. Such research, particularly when combined with complementary analytical methods, will enhance our understanding of hail formation mechanisms and help refine predictive models. As we continue to improve modeling efforts, incorporating diverse aerosol compositions and sizes will be crucial for enhancing the accuracy of forecasts related to hail events.

Data availability. The physical (CLSM) and chemical (EDS) data of the two analyzed hailstones are stored in an Excel sheet, which is accessible through Zenodo (https://doi.org/10.5281/zenodo.10455803, Bernal Ayala et al., 2024a). We obtained the ERA5 reanalysis data from Hersbach et al. (2023) (https://doi.org/10.24381/cds.bd0915c6) and the land cover classification gridded map from the Copernicus Climate Change Service (https://doi.org/10.24381/CDS.006F2C9A, Copernicus Climate Change Service, 2019). These ERA5 data were input to the National Oceanographic and Atmospheric Administration's Hybrid Single-Particle Lagrangian Integrated Trajectory (HYSPLIT) model (version 5.3.0; available at https://www.ready.noaa.gov/HYSPLIT.php, NOAA, 2025) to produce residence-time coefficient plots based on the air mass trajectories.

Author contributions. Conceptualization was carried out by ACBA and LEA; methodology was developed by ACBA, AKR, LEA, and WON; validation was performed by AKR, LEA, and WON; formal analysis was conducted by ACBA; the investigation was undertaken by ACBA, AKR, and LEA; resources were provided by AKR and LEA; LEA managed data curation; the original draft was prepared by ACBA; writing (review and editing) was done by ACBA, AKR, LEA, and WON; visualization was handled by ACBA; supervision was provided by AKR, LEA, and WON; and funding acquisition was secured by AKR. All authors have read and agreed to the published version of the manuscript.

Competing interests. The contact author has declared that none of the authors has any competing interests.

Acknowledgements. We would like to thank the LAMARX-UNC operators for their assistance in operating the microscopes used in this study, especially Sebastian Garcia, for his assistance during the initial development of the technique used in this study.

Financial support. This research has been supported by the National Science Foundation Division of Atmospheric and Geospace Sciences (grant nos. AGS-1640452 and AGS-1661768).

Review statement. This paper was edited by Daniel Knopf and reviewed by two anonymous referees.

References

Allen, J. T., Tippett, M. K., Kaheil, Y., Sobel, A. H., Lepore, C., Nong, S., and Muehlbauer, A.: An Extreme Value Model for U.S. Hail Size, Mon. Weather Rev., 145, 4501–4519, https://doi.org/10.1175/MWR-D-17-0119.1, 2017.

Allen, J. T., Giammanco, I. M., Kumjian, M. R., Jurgen Punge, H., Zhang, Q., Groenemeijer, P., Kunz, M., and Ortega, K.: Understanding Hail in the Earth System, Rev. Geophys., 58, e2019RG000665, https://doi.org/10.1029/2019RG000665, 2020.

Arena, L. and Crespo, A.: Recopilación de estudios primarios de caracterización cristalográfica de granizos y de las tormentas que los originan, Universidad Nacional de Córdoba, https://repositoriosdigitales.mincyt.gob.ar/vufind/Record/RDUUNC_35bc5a10fa9dbe231285cb6365785426 (last access: 18 October 2024), 2019.

Arena, L. E.: Cosecheros. Argentina.gob.ar, https://www.argentina.gob.ar/sites/default/files/cosecheros_de_granizo_cordoba.pdf (last access: 27 October 2023), 2022.

Arena, L. E.: Identificación de partículas incluidas en hielos naturales (glaciares, permafrost, granizo) por sublimación adaptada, Anales AFA, 35, 25–27, https://doi.org/10.31527/analesafa.2024.35.2.25, 2024.

Argentina, F.: ZINC 700, FMC Argentina, http://www.fmcargentina.com.ar/productos/zinc-700/ (last access: 19 September 2024), 2024.

Ashbaugh, L. L., Malm, W. C., and Sadeh, W. Z.: A Residence Time Probability Analysis of Sulfur Concentrations at Grand Canyon National Park, Atmos. Environ., 19, 1263–1270, 1985.

Bakan, S., Hinzpeter, H., Höller, H., Jaenicke, R., Jeske, H., Laube, M., Volland, H., Warneck, P., and Wurzinger, C.: Physical and Chemical Properties of the Air/Physikalische Und Chemische Eigenschaften Der Luft, in: vol. 4 Sub Vol B of Landolt-Börnstein: Numerical Data and Functional Relationships in Science and Technology – New Series, Springer, Berlin, Heidelberg, ISBN 3-540-17603-9, 1987.

Bang, S. D. and Cecil, D. J.: Constructing a Multifrequency Passive Microwave Hail Retrieval and Climatology in the GPM Domain, J. Appl. Meteorol. Clim., 58, 1889–1904, https://doi.org/10.1175/JAMC-D-19-0042.1, 2019.

Beal, A., Martins, L. D., Martins, J. A., Rudke, A. P., de Almeida, D. S., Costa, L. M., and Tarley, C. R. T.: Evaluation of the Chemical Composition of Hailstones from Triple Border Paraná, Santa Catarina (Brazil) and Argentina, Atmos. Pollut. Res., 12, 184–192, https://doi.org/10.1016/j.apr.2021.01.009, 2021.

Bernal Ayala, A. C., Rowe, A. K., Arena, L. E., and Desai, A. R.: Evaluation of Satellite-Derived Signatures for Three Verified Hailstorms in Central Argentina, Meteorology, 1, 183–210, https://doi.org/10.3390/meteorology1020013, 2022.

Bernal Ayala, A. C., Rowe, A., Arena, L. E., and Nachlas, W. O.: Individual Particle Dataset: Physical-chemical Properties of Non-Soluble Particles in a Hailstone Collected in Argentina, Zenodo [data set], https://doi.org/10.5281/zenodo.10455803, 2024a.

Bernal Ayala, A. C., Rowe, A. K., Arena, L. E., Nachlas, W. O., and Asar, M. L.: Exploring non-soluble particles in hailstones through innovative confocal laser and scanning electron microscopy techniques, Atmos. Meas. Tech., 17, 5561–5579, https://doi.org/10.5194/amt-17-5561-2024, 2024b.

Borda, L. G., Cosentino, N. J., Iturri, L. A., García, M. G., and Gaiero, D. M.: Is Dust Derived From Shrinking Saline Lakes a Risk to Soil Sodification in Southern South America?, J. Geophys. Res.-Earth, 127, e2021JF006585, https://doi.org/10.1029/2021JF006585, 2022.

Bruick, Z. S., Rassumen, K. L., and Cecil, D. J.: Subtropical South American Hailstorm Characteristics and Environments, Mon. Weather Rev., 147, 4289–4304, https://doi.org/10.1175/MWR-D-19-0011.1, 2019.

Burrows, S. M., McCluskey, C. S., Cornwell, G., Steinke, I., Zhang, K., Zhao, B., Zawadowicz, M., Raman, A., Kulkarni, G., China, S., Zelenyuk, A., and DeMott, P. J.: Ice-Nucleating Particles That Impact Clouds and Climate: Observational and Modeling Research Needs, Rev. Geophys., 60, e2021RG000745, https://doi.org/10.1029/2021RG000745, 2022.

Caburé, E.: Fertilizante foliar orgánico con acción insecticida, https://www.elcabureia.com/portfolio/items/fertilizante-foliar-organico-con-accion-insecticida (last access: 9 October 2024), 2024.

Cecil, D. J. and Blankenship, C. B.: Toward a Global Climatology of Severe Hailstorms as Estimated by Satellite Passive Microwave Imagers, J. Climate, 25, 687–703, https://doi.org/10.1175/JCLI-D-11-00130.1, 2012.

Changnon, S. A.: Temporal and Spatial Distributions of Damaging Hail in the Continental United States, Phys. Geogr., 29, 341–350, https://doi.org/10.2747/0272-3646.29.4.341, 2008.

Chen, J., Wu, Z., Chen, J., Reicher, N., Fang, X., Rudich, Y., and Hu, M.: Size-resolved atmospheric ice-nucleating particles during East Asian dust events, Atmos. Chem. Phys., 21, 3491–3506, https://doi.org/10.5194/acp-21-3491-2021, 2021.

Claquin, T., Schulz, M., and Balkanski, Y. J.: Modeling the Mineralogy of Atmospheric Dust Sources, J. Geophys. Res.-Atmos., 104, 22243–22256, https://doi.org/10.1029/1999JD900416, 1999.

Conen, F., Morris, C. E., Leifeld, J., Yakutin, M. V., and Alewell, C.: Biological Residues Define the Ice Nucleation Properties of Soil Dust, Atmos. Chem. Phys., 11, 9643–9648, https://doi.org/10.5194/acp-11-9643-2011, 2011.

Conny, J. M., Willis, R. D., and Ortiz-Montalvo, D. L.: Analysis and Optical Modeling of Individual Heterogeneous Asian Dust Particles Collected at Mauna Loa Observatory, J. Geophys. Res.-Atmos., 124, 2702–2723, https://doi.org/10.1029/2018JD029387, 2019.

Copernicus Climate Change Service: Land Cover Classification Gridded Maps from 1992 to Present Derived from Satellite Observations, Copernicus Climate Change Service (C3S) Climate Data Store (CDS) [data set], https://doi.org/10.24381/CDS.006F2C9A, 2019.

Cornwell, G. C., Steinke, I., Lata, N. N., Zelenyuk, A., Kulkarni, G., Pekour, M., Perkins, R., Levin, E. J. T., China, S., DeMott, P. J., and Burrows, S. M.: Enrichment of Phosphates, Lead, and Mixed Soil-Organic Particles in INPs at the Southern Great Plains Site, J. Geophys. Res.-Atmos., 129, e2024JD040826, https://doi.org/10.1029/2024JD040826, 2024.

Cziczo, D. J., Stetzer, O., Worringen, A., Ebert, M., Weinbruch, S., Kamphus, M., Gallavardin, S. J., Curtius, J., Borrmann, S., Froyd, K. D., Mertes, S., Möhler, O., and Lohmann, U.: Inadvertent Climate Modification Due to Anthropogenic Lead, Nat. Geosci., 2, 333–336, https://doi.org/10.1038/ngeo499, 2009.

DeMott, P. J. and Prenni, A. J.: New Directions: Need for Defining the Numbers and Sources of Biological Aerosols Acting as Ice Nuclei, Atmos. Environ., 44, 1944–1945, https://doi.org/10.1016/j.atmosenv.2010.02.032, 2010.

DeMott, P. J., Hill, T. C. J., McCluskey, C. S., Prather, K. A., Collins, D. B., Sullivan, R. C., Ruppel, M. J., Mason, R. H., Irish, V. E., Lee, T., Hwang, C. Y., Rhee, T. S., Snider, J. R., McMeeking, G. R., Dhaniyala, S., Lewis, E. R., Wentzell, J. J. B., Abbatt, J., Lee, C., Sultana, C. M., Ault, A. P., Axson, J. L., Martinez, M. D., Venero, I., Santos-Figueroa, G., Stokes, M. D., Deane, G. B., Mayol-Bracero, O. L., Grassian, V. H., Bertram, T. H., Bertram, A. K., Moffett, B. F., and Franc, G. D.: Sea Spray Aerosol as a Unique Source of Ice Nucleating Particles, P. Natl. Acad. Sci. USA, 113, 5797–5803, https://doi.org/10.1073/pnas.1514034112, 2016.

Di Biagio, C., Balkanski, Y., Albani, S., Boucher, O., and Formenti, P.: Direct Radiative Effect by Mineral Dust Aerosols Constrained by New Microphysical and Spectral

Optical Data, Geophys. Res. Lett., 47, e2019GL086186, https://doi.org/10.1029/2019GL086186, 2020.

Espeche, M. J. and Lira, R.: Ecandrewsite (ZnTiO3) in Amphibolites, Sierras de Córdoba, Argentina: Mineral Chemistry and Comparison with Different Worldwide Paragenetic Occurrences, Can. Mineralog., 60, 677–686, https://doi.org/10.3749/canmin.2100055, 2022.

Filmetrics: ProfilmOnline 3D Imaging and Analysis Software, https://www.kla.com/products/instruments/optical-profilers/profilm3d (last access: 6 July 2024), 2017.

Fletcher, C.: Physical Geology: The Science of Earth, Wiley, ISBN-13 9780471220374, 2011.

Gao, K., Zhou, C.-W., Meier, E. J. B., and Kanji, Z. A.: Laboratory studies of ice nucleation onto bare and internally mixed soot–sulfuric acid particles, Atmos. Chem. Phys., 22, 5331–5364, https://doi.org/10.5194/acp-22-5331-2022, 2022.

Goldstein, J. I., Newbury, D. E., Michael, J. R., Ritchie, N. W. M., Scott, J. H. J., and Joy, D. C.: Scanning Electron Microscopy and X-Ray Microanalysis, Springer, ISBN 978-1-4939-6676-9, 2017.

Grenier, J.-C. and Sadok Zair, P. A.: Hailstone Growth Trajectories in the Dynamic Evolution of a Moderate Hailstorm, J. Appl. Meteorol. Clim., 22, 1008–1021, https://doi.org/10.1175/1520-0450(1983)022<1008:HGTITD>2.0.CO;2, 1983.

Hersbach, H., Bell, B., Berrisford, P., Hirahara, S., Horányi, A., Muñoz-Sabater, J., Nicolas, J., Peubey, C., Radu, R., Schepers, D., Simmons, A., Soci, C., Abdalla, S., Abellan, X., Balsamo, G., Bechtold, P., Biavati, G., Bidlot, J., Bonavita, M., De Chiara, G., Dahlgren, P., Dee, D., Diamantakis, M., Dragani, R., Flemming, J., Forbes, R., Fuentes, M., Geer, A., Haimberger, L., Healy, S., Hogan, R. J., Hólm, E., Janisková, M., Keeley, S., Laloyaux, P., Lopez, P., Lupu, C., Radnoti, G., de Rosnay, P., Rozum, I., Vamborg, F., Villaume, S., and Thépaut, J.-N.: The ERA5 Global Reanalysis, Q. J. Roy. Meteorol. Soc., 146, 1999–2049, https://doi.org/10.1002/qj.3803, 2020.

Hersbach, H., Bell, B., Berrisford, P., Biavati, G., Horányi, A., Muñoz-Sabater, J., Nicolas, J., Peubey, C., Radu, R., Schepers, D., Simmons, A., Soci, C., Dee, D., and Thépaut, J.-N.: ERA5 Hourly Data on Pressure Levels from 1940 to Present, Copernicus Climate Change Service (C3S) Climate Data Store (CDS) [data set], https://doi.org/10.24381/cds.bd0915c6, 2023.

Heymsfield, A. J. and Pflaum, J. C.: A Quantitative Assessment of the Accuracy of Techniques for Calculating Graupel Growth, J. Atmos. Sci., 42, 2264–2274, https://doi.org/10.1175/1520-0469(1985)042<2264:AQAOTA>2.0.CO;2, 1985.

Holden, M. A., Campbell, J. M., Meldrum, F. C., Murray, B. J., and Christenson, H. K.: Active Sites for Ice Nucleation Differ Depending on Nucleation Mode, P. Natl. Acad. Sci. USA, 118, e2022859118, https://doi.org/10.1073/pnas.2022859118, 2021.

Huang, Y., Kok, J. F., Kandler, K., Lindqvist, H., Nousiainen, T., Sakai, T., Adebiyi, A., and Jokinen, O.: Climate Models and Remote Sensing Retrievals Neglect Substantial Desert Dust Asphericity, Geophys. Res. Lett., 47, e2019GL086592, https://doi.org/10.1029/2019GL086592, 2020.

International Trade Administration: Argentina – Mining, https://www.trade.gov/country-commercial-guides/argentina-mining (last access: 18 October 2024), 2023.

Iturri, L. A., Funk, R., Leue, M., Sommer, M., and Buschiazzo, D. E.: Wind Sorting Affects Differently the Organo-Mineral Composition of Saltating and Particulate Materials in Contrasting Texture Agricultural Soils, Aeolian Res., 28, 39–49, https://doi.org/10.1016/j.aeolia.2017.07.005, 2017.

Jaenicke, R.: Physical Properties of Atmospheric Particulate Sulfur Compounds, Atmos. Environ., 12, 161–169, https://doi.org/10.1016/0004-6981(78)90197-X, 1978.

Jeong, G. Y. and Achterberg, E. P.: Chemistry and mineralogy of clay minerals in Asian and Saharan dusts and the implications for iron supply to the oceans, Atmos. Chem. Phys., 14, 12415–12428, https://doi.org/10.5194/acp-14-12415-2014, 2014.

Jeong, G. Y. and Nousiainen, T.: TEM analysis of the internal structures and mineralogy of Asian dust particles and the implications for optical modeling, Atmos. Chem. Phys., 14, 7233–7254, https://doi.org/10.5194/acp-14-7233-2014, 2014.

Jeong, G. Y., Park, M. Y., Kandler, K., Nousiainen, T., and Kemppinen, O.: Mineralogical properties and internal structures of individual fine particles of Saharan dust, Atmos. Chem. Phys., 16, 12397–12410, https://doi.org/10.5194/acp-16-12397-2016, 2016.

Kandler, K., Benker, N., Bundke, U., Cuevas, E., Ebert, M., Knippertz, P., Rodríguez, S., Schütz, L., and Weinbruch, S.: Chemical Composition and Complex Refractive Index of Saharan Mineral Dust at Izaña, Tenerife (Spain) Derived by Electron Microscopy, Atmos. Environ., 41, 8058–8074, https://doi.org/10.1016/j.atmosenv.2007.06.047, 2007.

Kanji, Z. A., Ladino, L. A., Wex, H., Boose, Y., Burkert-Kohn, M., Cziczo, D. J., and Krämer, M.: Overview of Ice Nucleating Particles, Meteorol. Monogr., 58, 1.1–1.33, https://doi.org/10.1175/AMSMONOGRAPHS-D-16-0006.1, 2017.

Kemppinen, O., Nousiainen, T., and Jeong, G. Y.: Effects of dust particle internal structure on light scattering, Atmos. Chem. Phys., 15, 12011–12027, https://doi.org/10.5194/acp-15-12011-2015, 2015.

Kiselev, A., Bachmann, F., Pedevilla, P., Cox, S. J., Michaelides, A., Gerthsen, D., and Leisner, T.: Active Sites in Heterogeneous Ice Nucleation, the Example of K-rich Feldspars, Science, 355, 367–371, https://doi.org/10.1126/science.aai8034, 2017.

Knopf, D. A., Alpert, P. A., and Wang, B.: The Role of Organic Aerosol in Atmospheric Ice Nucleation: A Review, ACS Earth Space Chem., 2, 168–202, https://doi.org/10.1021/acsearthspacechem.7b00120, 2018.

Kozjek, M., Vengust, D., Radošević, T., Žitko, G., Koren, S., Toplak, N., Jerman, I., Butala, M., Podlogar, M., and Viršek, M. K.: Dissecting Giant Hailstones: A Glimpse into the Troposphere with Its Diverse Bacterial Communities and Fibrous Microplastics, Sci. Total Environ., 856, 158786, https://doi.org/10.1016/j.scitotenv.2022.158786, 2023.

Kumjian, M. R. and Lombardo, K.: A Hail Growth Trajectory Model for Exploring the Environmental Controls on Hail Size: Model Physics and Idealized Tests, J. Atmos. Sci., 77, 2765–2791, https://doi.org/10.1175/JAS-D-20-0016.1, 2020.

Kumjian, M. R., Lebo, Z. J., and Ward, A. M.: Storms Producing Large Accumulations of Small Hail, J. Appl. Meteorol. Clim., 58, 341–364, https://doi.org/10.1175/JAMC-D-18-0073.1, 2019.

Kumjian, M. R., Gutierrez, R., Soderholm, J. S., Nesbitt, S. W., Maldonado, P., Luna, L. M., Marquis, J., Bowley, K. A., Imaz, M. A., and Salio, P.: Gargantuan Hail in Argentina, B. Am. Meteorol. Soc., 101, E1241–E1258, https://doi.org/10.1175/BAMS-D-19-0012.1, 2020.

Lamb, D. and Verlinde, J.: Physics and Chemistry of Clouds, Cambridge University Press, Cambridge, ISBN 978-0-521-89910-9, https://doi.org/10.1017/CBO9780511976377, 2011.

Levi, L., Lubart, L., Nasello, O. B., and Arena, L.: Analysis of a Hailstorm Ocurred in Alta Gracia Cordoba, Argentina, in: Third International Conference on Southern Hemisphere Meteorology and Oceanography, 13–17 November 1989, Buenos Aires, Argentina, 343 pp., https://www.jstor.org/stable/26227436 (last access: 2 April 2025), 1989.

Levi, L., Arena, L., Nasello, O., and Lubart, L.: Condiciones Iniciales de Crecimiento de Granizos Gigantes, in: CONGREMET VI, Anales del Centro Argentino de Meterologìa, Buenos Aires, Argentina, 23–27, 1991.

Lewis, K. A., Tzilivakis, J., Warner, D. J., and Green, A.: An International Database for Pesticide Risk Assessments and Management, Hum. Ecol. Risk Assess., 22, 1050–1064, https://doi.org/10.1080/10807039.2015.1133242, 2016.

Li, L. and Sokolik, I. N.: The Dust Direct Radiative Impact and Its Sensitivity to the Land Surface State and Key Minerals in the WRF-Chem-DuMo Model: A Case Study of Dust Storms in Central Asia, J. Geophys. Res.-Atmos., 123, 4564–4582, https://doi.org/10.1029/2017JD027667, 2018.

Lubart, L. and Levi, L.: Crecimiento de Embriones de Granizo de Tipo “Graupel”, Geoacta, 12, 157–168, 1984.

Mahoney, K.: Extreme Hail Storms and Climate Change: Foretelling the Future in Tiny, Turbulent Crystal Balls?, B. Am. Meteorol. Soc., 101, S17–S22, https://doi.org/10.1175/BAMS-D-19-0233.1, 2020.

Manoj, P.: Copper Oxychloride Market Report 2024 (Global Edition), Tech. Rep. CMR767910, Cognitive Market Research, https://www.cognitivemarketresearch.com/copper-oxychloride-market-report (last access: 9 February 2024), 2023.

Michaud, A. B., Dore, J. E., Leslie, D., Lyons, W. B., Sands, D. C., and Priscu, J. C.: Biological Ice Nucleation Initiates Hailstone Formation, J. Geophys. Res.-Atmos., 119, 12186–12197, https://doi.org/10.1002/2014JD022004, 2014.

Mokkapati, S. P.: Simulation of Particle Agglomeration Using Dissipative Particle Dynamics, PhD thesis, https://hdl.handle.net/1969.1/ETD-TAMU-1149 (last access: 9 March 2025), 2009.

Mulholland, J. P., Nesbitt, S. W., Trapp, R. J., Rasmussen, K. L., and Salio, P. V.: Convective Storm Life Cycle and Environments near the Sierras de Córdoba, Argentina, Mon. Weather Rev., 146, 2541–2557, https://doi.org/10.1175/MWR-D-18-0081.1, 2018.

Murillo, E. M. and Homeyer, C. R.: Severe Hail Fall and Hailstorm Detection Using Remote Sensing Observations, J. Appl. Meteorol. Clim., 58, 947–970, https://doi.org/10.1175/JAMC-D-18-0247.1, 2019.

Nesbitt, S. W., Salio, P. V., Ávila, E., Bitzer, P., Carey, L., Chandrasekar, V., Deierling, W., Dominguez, F., Dillon, M. E., Garcia, C. M., Gochis, D., Goodman, S., Hence, D. A., Kosiba, K. A., Kumjian, M. R., Lang, T., Luna, L. M., Marquis, J., Marshall, R., McMurdie, L. A., Nascimento, E. D. L., Rasmussen, K. L., Roberts, R., Rowe, A. K., Ruiz, J. J., Sabbas, E. F. M. T. S., Saulo, A. C., Schumacher, R. S., Skabar, Y. G., Machado, L. A. T., Trapp, R. J., Varble, A. C., Wilson, J., Wurman, J., Zipser, E. J., Arias, I., Bechis, H., and Grover, M. A.: A Storm Safari in Subtropical South America: Proyecto RELAMPAGO, B. Am. Meteorol. Soc., 102, E1621–E1644, https://doi.org/10.1175/BAMS-D-20-0029.1, 2021.

Ni, X., Liu, C., Cecil, D. J., and Zhang, Q.: On the Detection of Hail Using Satellite Passive Microwave Radiometers and Precipitation Radar, J. Appl. Meteorol. Climatol., 56, 2693–2709, https://doi.org/10.1175/JAMC-D-17-0065.1, 2017.

NOAA: HYSPLIT, https://www.ready.noaa.gov/HYSPLIT.php (last access: 14 July 2025), 2025.

Nousiainen, T., Zubko, E., Niemi, J. V., Kupiainen, K., Lehtinen, M., Muinonen, K., and Videen, G.: Single-Scattering Modeling of Thin, Birefringent Mineral-Dust Flakes Using the Discrete-Dipole Approximation, J. Geophys. Res.-Atmos., 114, D07207, https://doi.org/10.1029/2008JD011564, 2009.

Pruppacher, H. R. and Klett, J. D.: Microphysics of Clouds and Precipitation, in: vol. 18, Springer Netherlands, ISBN 978-0-7923-4211-3, 1980.

Rangno, A. L. and Hobbs, P. V.: Ice Particle Concentrations and Precipitation Development in Small Polar Maritime Cumuliform Clouds, Q. J. Roy. Meteorol. Soc., 117, 207–241, https://doi.org/10.1002/qj.49711749710, 1991.

Rasmussen, K. L. and Houze, Jr., R. A.: Convective Initiation near the Andes in Subtropical South America, Mon. Weather Rev., 144, 2351–2374, https://doi.org/10.1175/MWR-D-15-0058.1, 2016.

Rasmussen, K. L., Zuluaga, M. D., and Houze Jr., R. A.: Severe Convection and Lightning in Subtropical South America, Geophys. Res. Lett., 41, 7359–7366, https://doi.org/10.1002/2014GL061767, 2014.

Raupach, T. H., Martius, O., Allen, J. T., Kunz, M., Lasher-Trapp, S., Mohr, S., Rasmussen, K. L., Trapp, R. J., and Zhang, Q.: The Effects of Climate Change on Hailstorms, Nat. Rev. Earth Environ., 2, 213–226, https://doi.org/10.1038/s43017-020-00133-9, 2021.

Ren, L., Yang, Y., Wang, H., Wang, P., Chen, L., Zhu, J., and Liao, H.: Aerosol transport pathways and source attribution in China during the COVID-19 outbreak, Atmos. Chem. Phys., 21, 15431–15445, https://doi.org/10.5194/acp-21-15431-2021, 2021.

Rizobacter: Status ZN, https://rizobacter.com.ar/es/productos/argentina/status-zn (last access: 19 September 2024), 2024.

Sander, J., Eichner, J. F., Faust, E., and Steuer, M.: Rising Variability in Thunderstorm-Related U.S. Losses as a Reflection of Changes in Large-Scale Thunderstorm Forcing, Weather Clim. Soc., 5, 317–331, https://doi.org/10.1175/WCAS-D-12-00023.1, 2013.

Šantl-Temkiv, T., Finster, K., Dittmar, T., Hansen, B. M., Thyrhaug, R., Nielsen, N. W., and Karlson, U. G.: Hailstones: A Window into the Microbial and Chemical Inventory of a Storm Cloud, PLOS ONE, 8, 1–7, https://doi.org/10.1371/journal.pone.0053550, 2013.

Sasaki, C. R. S., Rowe, A. K., McMurdie, L. A., and Rasmussen, K. L.: New Insights into the South American Low-Level Jet from RELAMPAGO Observations, Mon. Weather Rev., 150, 1247–1271, https://doi.org/10.1175/MWR-D-21-0161.1, 2022.

Sasaki, C. R. S., Rowe, A. K., McMurdie, L. A., Varble, A. C., and Zhang, Z.: Influences of the South American Low-Level Jet on the Convective Environment in Central Argentina Using a Convection-Permitting Simulation, Mon. Weather Rev., 152, 629–648, https://doi.org/10.1175/MWR-D-23-0122.1, 2024.

Schütz, L. and Sebert, M.: Mineral Aerosols and Source Identification, J. Aerosol Sci., 18, 1–10, https://doi.org/10.1016/0021-8502(87)90002-4, 1987.

Soderholm, J. S. and Kumjian, M. R.: Automating the analysis of hailstone layers, Atmos. Meas. Tech., 16, 695–706, https://doi.org/10.5194/amt-16-695-2023, 2023.

Sokolik, I. N. and Toon, O. B.: Direct Radiative Forcing by Anthropogenic Airborne Mineral Aerosols, Nature, 381, 681–683, https://doi.org/10.1038/381681a0, 1996.

Sokolik, I. N. and Toon, O. B.: Incorporation of Mineralogical Composition into Models of the Radiative Properties of Mineral Aerosol from UV to IR Wavelengths, J. Geophys. Res.-Atmos., 104, 9423–9444, https://doi.org/10.1029/1998JD200048, 1999.

SRL: Fábrica de fertilizantes|Recuperar S.R.L.|Córdoba, https://www.recuperarsrl.com.ar (last access: 9 October 2024), 2021.

Stein, A. F., Draxler, R. R., Rolph, G. D., Stunder, B. J. B., Cohen, M. D., and Ngan, F.: NOAA's HYSPLIT Atmospheric Transport and Dispersion Modeling System, B. Am. Meteorol. Soc., 96, 2059–2077, https://doi.org/10.1175/BAMS-D-14-00110.1, 2015.

Steinke, I., Funk, R., Busse, J., Iturri, A., Kirchen, S., Leue, M., Möhler, O., Schwartz, T., Schnaiter, M., Sierau, B., Toprak, E., Ullrich, R., Ulrich, A., Hoose, C., and Leisner, T.: Ice Nucleation Activity of Agricultural Soil Dust Aerosols from Mongolia, Argentina, and Germany, J. Geophys. Res.-Atmos., 121, 13559–13576, https://doi.org/10.1002/2016JD025160, 2016.

Takahashi, T.: Hawaiian Hailstones – 30 January 1985, B. Am. Meteorol. Soc., 68, 1530–1534, https://doi.org/10.1175/1520-0477(1987)068<1530:HHJ>2.0.CO;2, 1987.

Tarn, M. D., Sikora, S. N. F., Porter, G. C. E., O'Sullivan, D., Adams, M., Whale, T. F., Harrison, A. D., Vergara-Temprado, J., Wilson, T. W., Shim, J.-U., and Murray, B. J.: The Study of Atmospheric Ice-Nucleating Particles via Microfluidically Generated Droplets, Microfluid Nanofluid., 22, 52, https://doi.org/10.1007/s10404-018-2069-x, 2018.

Tegen, I. and Lacis, A. A.: Modeling of Particle Size Distribution and Its Influence on the Radiative Properties of Mineral Dust Aerosol, J. Geophys. Res.-Atmos., 101, 19237–19244, https://doi.org/10.1029/95JD03610, 1996.

Testa, B., Hill, T. C. J., Marsden, N. A., Barry, K. R., Hume, C. C., Bian, Q., Uetake, J., Hare, H., Perkins, R. J., Möhler, O., Kreidenweis, S. M., and DeMott, P. J.: Ice Nucleating Particle Connections to Regional Argentinian Land Surface Emissions and Weather During the Cloud, Aerosol, and Complex Terrain Interactions Experiment, J. Geophys. Res.-Atmos., 126, e2021JD035186, https://doi.org/10.1029/2021JD035186, 2021.

USGS: Minerals Yearbook, 2017–2018, Latin American And Canada, in: vol. 111, US Government Publishing Office, ISBN 978-1-4113-4231-6, 2019.

Vali, G., DeMott, P. J., Möhler, O., and Whale, T. F.: Technical Note: A proposal for ice nucleation terminology, Atmos. Chem. Phys., 15, 10263–10270, https://doi.org/10.5194/acp-15-10263-2015, 2015.

Varble, A. C., Nesbitt, S. W., Salio, P., Hardin, J. C., Bharadwaj, N., Borque, P., DeMott, P. J., Feng, Z., Hill, T. C. J., Marquis, J. N., Matthews, A., Mei, F., Öktem, R., Castro, V., Goldberger, L., Hunzinger, A., Barry, K. R., Kreidenweis, S. M., McFarquhar, G. M., McMurdie, L. A., Pekour, M., Powers, H., Romps, D. M., Saulo, C., Schmid, B., Tomlinson, J. M., van den Heever, S. C., Zelenyuk, A., Zhang, Z., and Zipser, E. J.: Utilizing a Storm-Generating Hotspot to Study Convective Cloud Transitions: The CACTI Experiment, B. Am. Meteorol. Soc., 102, E1597–E1620, https://doi.org/10.1175/BAMS-D-20-0030.1, 2021.

Wang, S., Mu, L., Wang, C., Li, X., Xie, J., Shang, Y., Pu, H., and Dong, M.: Modeling and Simulation of Micron Particle Agglomeration in a Turbulent Flow: Impact of Cylindrical Disturbance and Particle Properties, ACS Omega, 9, 49302–49315, https://doi.org/10.1021/acsomega.4c06441, 2024.

Yadav, S. K., Kompalli, S. K., Gurjar, B. R., and Mishra, R. K.: Aerosol Number Concentrations and New Particle Formation Events over a Polluted Megacity during the COVID-19 Lockdown, Atmos. Environ., 259, 118526, https://doi.org/10.1016/j.atmosenv.2021.118526, 2021.

Zaccarini, F., Garuti, G., Ortiz-Suarez, A., and Carugno-Duran, A.: The paragenesis of pyrophanite from Sierra de Comechingones, Córdoba, Argentina, Can. Mineralog., 42, 155–168, https://doi.org/10.2113/gscanmin.42.1.155, 2004.

Zhang, H., Lin, X., Zhang, Q., Bi, K., Ng, C.-P., Ren, Y., Xue, H., Chen, L., and Chang, Z.: Analysis of insoluble particles in hailstones in China, Atmos. Chem. Phys., 23, 13957–13971, https://doi.org/10.5194/acp-23-13957-2023, 2023.

Zhao, B., Wang, Y., Gu, Y., Liou, K.-N., Jiang, J. H., Fan, J., Liu, X., Huang, L., and Yung, Y. L.: Ice Nucleation by Aerosols from Anthropogenic Pollution, Nat. Geosci., 12, 602–607, https://doi.org/10.1038/s41561-019-0389-4, 2019.

Zipser, E. J., Nesbitt, S. W., Liu, C., and Yorty, D. P.: Where Are the Most Intense Thunderstorms on Earth?, B. Am. Meteorol. Soc., 87, 1057–1071, https://doi.org/10.1175/BAMS-87-8-1057, 2006.